

AD-A062 239

UTAH STATE UNIV LOGAN SPACE SCIENCE LAB
DEVELOPMENT OF A ROCKET-BORNE RESONANCE LAMP SYSTEM FOR THE MEA--ETC(U)
AUG 77 L C HOWLETT, K D BAKER

F/G 7/4

F19628-74-C-0130

UNCLASSIFIED

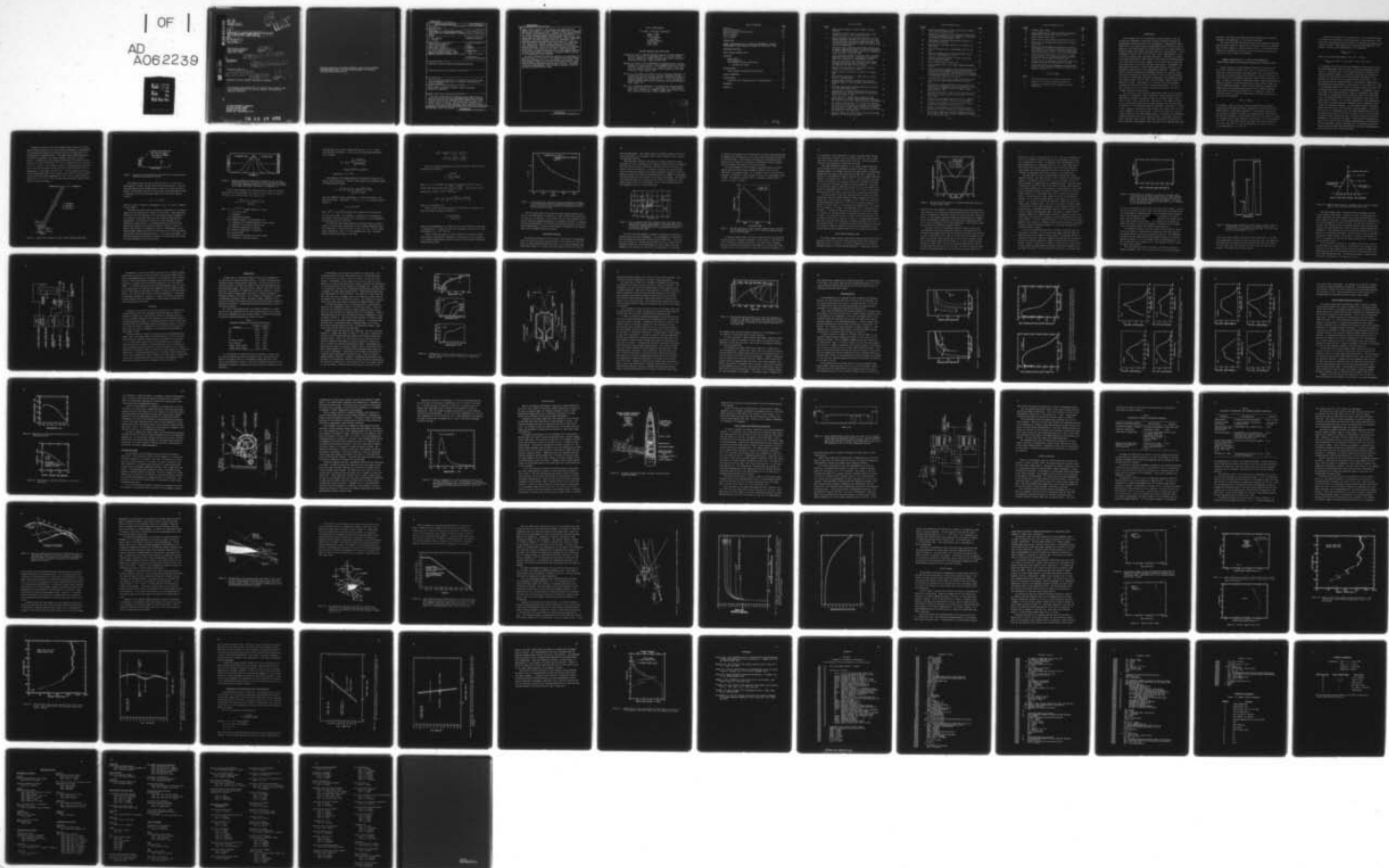
SCIENTIFIC-5

AFGL-TR-77-0227

NL

| OF |

AD
A062239



AD A062239

DDC FILE COPY

(18) (19)
AFGL TR-77-0227

(6)

DEVELOPMENT OF A ROCKET-BORNE RESONANCE LAMP SYSTEM
FOR THE MEASUREMENT OF ATOMIC OXYGEN

(10)
L. Carl/Howlett
Kay D./Baker

Space Science Laboratory
Utah State University
Logan, Utah 84322

(12) 87p.

(15) F19628-74-C-0130

(11) August 1977

(14) SCIENTIFIC-5

Scientific Report No. 5

(16) 7670, 43AAXH

(17) 10 X604

DDC
RECEIVED
DEC 18 1978
A

Approved for public release; distribution unlimited.

This research was sponsored by the Defense Nuclear Agency under
Subtask 43AAXHX604, Work Unit 02, entitled, "Ionization and
Reaction Chemistry."

AIR FORCE GEOPHYSICS LABORATORY
AIR FORCE SYSTEMS COMMAND
UNITED STATES AIR FORCE
HANSCOM AFB, MASSACHUSETTS 01731

✓ 407 724 78. 12 18 003 7073

Qualified requestors may obtain additional copies from the Defense Documentation Center. All others should apply to the National Technical Information Service.

UNCLASSIFIED

SECURITY CLASSIFICATION OF THIS PAGE (When Data Entered)

REPORT DOCUMENTATION PAGE		READ INSTRUCTIONS BEFORE COMPLETING FORM
1. REPORT NUMBER AFGL-TR-77-0227 ✓	2. GOVT ACCESSION NO.	3. RECIPIENT'S CATALOG NUMBER
4. TITLE (and Subtitle) DEVELOPMENT OF A ROCKET-BORNE RESONANCE LAMP SYSTEM FOR THE MEASUREMENT OF ATOMIC OXYGEN	5. TYPE OF REPORT & PERIOD COVERED Scientific Report No. 5 ✓	6. PERFORMING ORG. REPORT NUMBER
7. AUTHOR(s) L. Carl Howlett K. D. Baker	8. CONTRACT OR GRANT NUMBER(s) F19628-74-C-0130 ✓	
9. PERFORMING ORGANIZATION NAME AND ADDRESS Space Science Laboratory Utah State University Logan, Utah 84322	10. PROGRAM ELEMENT, PROJECT, TASK AREA & WORK UNIT NUMBERS 62101F 76701004	
11. CONTROLLING OFFICE NAME AND ADDRESS Air Force Geophysics Laboratory Hanscom AFB, Massachusetts 01731 Monitor / Thomas D. Conley / OPR	12. REPORT DATE August 1977	13. NUMBER OF PAGES 88
14. MONITORING AGENCY NAME & ADDRESS (if different from Controlling Office)	15. SECURITY CLASS (of this report) Unclassified	15a. DECLASSIFICATION DOWNGRADING SCHEDULE
16. DISTRIBUTION STATEMENT (of this Report) Approved for public release; distribution unlimited.		
17. DISTRIBUTION STATEMENT (of the abstract entered in Block 20, if different from Report)		
18. SUPPLEMENTARY NOTES This research was sponsored by the Defense Nuclear Agency under Subtask 43AAXHX604 Work Unit 02 entitled, "Ionization and Reaction Chemistry."		
19. KEY WORDS (Continue on reverse side if necessary and identify by block number) Atomic oxygen, resonant scattering, vacuum ultraviolet, mesospheric composition		
20. ABSTRACT (Continue on reverse side if necessary and identify by block number) Two small rocket payloads containing atomic oxygen resonance lamps and detectors were flown from White Sands during twilight and night conditions on 2 December 1975, to measure atomic oxygen profiles from 70 to 130 km. The payloads each consisted of a closed, flowing rf excited, modulated, oxygen resonance lamp pro- ducing on the order of 10^{13} photons/sec sr of 130.2, 130.4, 130.6 nm		

DD FORM 1 JAN 73 1473 EDITION OF 1 NOV 65 IS OBSOLETE

UNCLASSIFIED
SECURITY CLASSIFICATION OF THIS PAGE (When Data Entered)

10 to the 13th power

UNCLASSIFIED

SECURITY CLASSIFICATION OF THIS PAGE(When Data Entered)

alpha

oxygen triplet radiation. The emissions were generated with minimal self reversal. The lamp output was baffled into a beam 38° deg wide normal to the payload axis. A segment of this beam was viewed by a photon counting detector designed for good sensitivity at 130 nm while rejecting Lyman-α and wavelengths beyond 130 nm. The system absolute calibration was achieved by two totally independent techniques. The first technique required a knowledge of all physical parameters associated with the system; i.e., lamp intensity, directivity, spectrum, atomic oxygen scattering cross section, temperatures, overall instrument geometry, and detector quantum efficiency. The second technique utilized the measurement of zenith 5577 nm intensity at the time of launch and an atmospheric model to place the absolute scale on the measured relative O profile. Preliminary calculations of absolute numbers from the two techniques are in good agreement.

The night instrument provided the capability for measurement of densities from $\sim 1 \times 10^8$ to 5×10^{12} atoms/cm³ and the day instrument was approximately an order of magnitude less sensitive. The night payload in particular provided a well-defined atomic oxygen profile showing significant upper D-region structure. Two peaks occurring at approximately 91 and 98 km were apparent in both up and down leg data from this flight.

UNCLASSIFIED

SECURITY CLASSIFICATION OF THIS PAGE(When Data Entered)

LIST OF CONTRIBUTORS

K.D. Baker - Principal Investigator

Doran J. Baker
David A. Burt
L. Carl Howlett
L. Rex Megill
William Pendleton
Larry Sharp
Alan W. Shaw

RELATED CONTRACTS AND PUBLICATIONS

Grieder, W.F. and L.A. Whelan, Geometric aspects of rocket photometry, *Scientific Report No. 3*, HAES Report No. 41, AFGL-TR-76-0046, 107 pp., Contract No. F19628-74-C-0130, Space Science Laboratory Utah State University, Logan, February 1976.

Howlett, L.C. and R.J. Bell, Rocketborne instrumentation for the measurement of electric fields - Paiute Tomahawk 10.312-3, *Scientific Report No. 2*, HAES Report No. 11, AFCRL-TR-75-0023, 91 pp., Contract No. F19628-74-C-0130, Space Science Laboratory, Utah State University, Logan, January 1975.

McCue, R.A., K.D. Baker, R.D. Harris, and C.D. Westlund, Measurement of D-region electron densities and collision frequencies at high northern latitudes by a Faraday rotation - differential absorption rocket experiment, *Scientific Report No. 4*, 97 pp., Contract No. F19628-74-C-0130, Space Science Laboratory, Utah State University, Logan, August 1977.

Neal, P.C., Design and calibration of a rocket-borne electron spectrometer, *Scientific Report No. 1*, HAES Report No. 8, AFCRL-TR-74-0629, 78 pp., Contract No. F19628-74-C-0130, Space Science Laboratory, Utah State University, Logan, December 1974.

ADDITIONAL INFO	
WITH	White Section <input checked="" type="checkbox"/>
ALL	Buff Section <input type="checkbox"/>
UNCLASSIFIED	<input type="checkbox"/>
REPRODUCTION	
BY	
DISTRIBUTION AVAILABILITY CODES	
U.S.	AVAIL. AND SPECIAL
A	

TABLE OF CONTENTS

	<u>Page</u>
Abstract	i
List of Contributors	iii
Related Contracts and Publications	iii
Table of Contents	v
List of Figures.	vii
List of Tables	ix
 INTRODUCTION.	 1
 GENERAL CONSIDERATIONS OF A SYSTEM FOR MEASUREMENT OF ATOMIC OXYGEN DENSITY USING RESONANT SCATTERING OF ULTRAVIOLET LIGHT .	 2
 BACKGROUND RADIATION	 9
 ATOMIC OXYGEN RESONANCE LAMP	 12
 DETECTORS.	 19
Geiger Tubes	20
Photomultipliers.	26
Curved Channel Electron Multipliers	31
CEM detector design	33
 PAYLOAD DESIGN	 37
Atomic Oxygen Instrumentation Electronics	39
 SYSTEM CALIBRATION.	 42
 FLIGHT RESULTS	 55
Comparison with Ground-based 557.7 nm Measurements	62
 REFERENCES	 67
 APPENDIX A	 69

LIST OF FIGURES

<u>Figure</u>		<u>Page</u>
1	Energy level diagram for atomic oxygen resonance emission	4
2	Idealized O triplet emission spectrum with no self-absorption and 5:3:1 line intensity ratios.	5
3	Doppler-broadened low temperature absorption line and higher temperature emission line typical of the conditions anticipated in an atomic oxygen measurement where the lamp emission temperature exceeds the ambient temperature of atmospheric O.	6
4	Correction factor resulting from unequal emission and absorption temperatures based on an emission temperature of 1600°K, Doppler line shapes, and no self-absorption either inside or outside the lamp.	9
5	Solar ultraviolet spectral irradiance above the Earth's atmosphere observed with a photographic spectrograph (NRL) and a photoelectric monochromator (AFCRC)	10
6	Smoothed experimental 1304 intensity height profile including the low tube data of <i>Fastie et al.</i> [1964] and high altitude data of <i>Fastie</i> [1968].	11
7	Measured altitude profiles of prominent emissions from N ₂ , H, N, and O [<i>Peek</i> , 1970].	13
8	Typical start-up transient in an Xonics O resonance lamp	15
9	Measured lamp spectrum for a lamp typical of those flown for O measurements.	16
10	Measured lamp intensity O emissions from an Xonics resonance lamp as a function angle from lamp optical axis	17
11	Resonance lamp system including lamp control, excitation, and monitoring process	18
12	Transmittance of various window materials for use in the VUV with CaF and LiF being shown as functions of temperature [<i>Samson</i> , 1967]	22
13	Cross section of a Geiger tube designed for high sensitivity to O resonance radiation while having very low sensitivities to both longer and shorter wavelengths	23
14	The recovery characteristics of a Geiger tube showing as a function of time from a proceeding count the period of time in which no additional count may be initiated, and the period of time in which a count may be initiated but which has a lower amplitude	25
15	Spectral response of various alkali halide photocathode materials in the vacuum ultraviolet	27

LIST OF FIGURES (cont.)

<u>Figure</u>		<u>Page</u>
16	Overall photomultiplier response published by EMR for solar blind photomultipliers.	28
17	Photoelectric yields of various materials likely to be found in photomultipliers as a function of wavelength with normal incidence [Samson, 1967]	29
18	Manufacturer's published CEM quantum efficiency in the vacuum ultraviolet.	32
19	Manufacturer's published CEM gain as a function of count rate.	32
20	View of CEM detector for O measurement with lid cut away.	34
21	Spectral transmission of a VUV interference filter built on a CaF ₂ substrate at 78 F	36
22	Astrobees D payload carrying a resonant scattering atomic oxygen measurement.	38
23	Hybrid PCM/PAM digital format used.	40
24	Block diagram of the flight atomic oxygen measurement system	41
25	Since the potential gradient along the CEM entrance cone is nonlinear with distance and the lower gradient is nearest to the cone mouth, the probability of producing a photoelectron which will fail to initiate an avalanche is considerably higher near the mouth.	46
26	Intersection of two conical fields, one from the light source and the second being the detection field of view.	48
27	The regions of partial occlusion may be treated by an analysis of the throughput from two apertures as a point light source at infinity travels through an angle θ varying from 0 to 90°	49
28	Calculated variation of lamp intensity as a function of angle due to partial occlusion by the baffle in front of the lamp	50
29	Detail of the coordinate system used for the computer evaluation of the atomic oxygen scattering geometry	52
30	Integral of contribution to count rate per O atoms as a function of distance from the detector.	53
31	Relative system response as a function of O density showing the effects of absorption at higher densities	54
32	Upleg atomic oxygen raw data with background subtracted for Astrobees D A30.413-4 launched at WSMR on 2 December 1975 at 19:00 local time	57

LIST OF FIGURES (cont.)

<u>Figure</u>		<u>Page</u>
33	Downleg atomic oxygen.	57
34	Atomic oxygen data in terms of 0 density showing an estimation of relative and absolute errors.	58
35	Atomic oxygen descent data	58
36	High resolution data showing considerable structure.	59
37	High resolution downleg data showing less structure than upleg	60
38	Statistical significance of 84 km dip in 0 density illustrated by $\pm 1\sigma$ limits in 0 density based on count rate statistics and a smooth curve which might have been expected which is many σ outside the measurement	61
39	Illustration of significance of structure in upleg profile based on far too many data points existing outside $\pm 1\sigma$ from a smooth anticipated curve	63
40	Illustration of the absence of any statistically significant structure in 0 density above the peak	64
41	Volume emission rate and integrated column intensity of 557.7 nm $O(^1S)$ radiation during the flight time of Astrobe D A30.413-4	66

LIST OF TABLES

<u>Table</u>		<u>Page</u>
1	Ionization potentials for Geiger filling gases	20
2	Evaluation of resonant scattering parameters	43
3	Evaluation of geometrical and component response parameters	44

INTRODUCTION

Atomic oxygen, due to its exceptionally reactive nature, is an important minor atmospheric constituent from the stratosphere through the mesosphere and lower portions of the thermosphere. Measurement of atomic oxygen within this region becomes challenging because of the difficulty in measuring a very small quantity of atomic oxygen in a very large quantity of molecular oxygen and nitrogen, and again due to its reactive nature. At approximately 75 km the ratio of $[O]$ to $[N_2] + [O_2]$ is approximately 1 part in 10^7 (the brackets denote the number densities). Obviously, to successfully measure mesospheric atomic oxygen a technique must be developed which is not only sensitive to atomic oxygen, but the effects must be separable from effects due to other major and minor constituents. Furthermore, the sharp spatial gradients in atomic oxygen number density occurring in the mesosphere strongly favor *in situ* measurement techniques. Inasmuch as the only practical mesospheric measurement platform is a sounding rocket which will be moving with typical velocities of one to several kilometers per second, the measurement technique must generate strong signals having fast response times, very low noise, and wide dynamic range (4 orders of magnitude or more). Furthermore, it is desirable that the measurement technique be insensitive to vehicle attitude and dynamics. For use on small rockets and in other combined rocket payloads, small size and instrument simplicity are important.

The technique at this time that appears best suited for the accurate measurement of mesospheric atomic oxygen with a simple system is based on measuring the resonant scattering of light in the atomic oxygen triplet lines at 130.2, 130.5, and 130.6 nm. The source of the resonance triplet is an on-board modulated RF excited oxygen resonance lamp with the output collimated into a beam impinging upon the atmosphere. A portion of the beam is then resonantly scattered by atomic oxygen into a photon detector which views a segment of the generated beam. The detector count rate is nearly linearly related to the atomic oxygen density. Fortunately, the absorption/reemission cross-section for the oxygen triplet is very large, which provides a generous return signal. The large cross-section also greatly reduces difficulty from competing light processes such as Rayleigh scattering

from major constituents and background airglow emissions (or scattered sunlight if the measurement is to be made in daylight).

This report discusses the physical basis for the resonant scattering technique and presents the design of the system utilized for the measurement of atomic oxygen in a small Astorbee D rocket. The calibration procedure and an estimate of its accuracy will be included, along with the results of the two flights of the system.

GENERAL CONSIDERATIONS OF A SYSTEM FOR MEASUREMENT OF ATOMIC OXYGEN DENSITY USING RESONANT SCATTERING OF ULTRAVIOLET LIGHT

Atomic oxygen has a strong resonant emission in the near vacuum ultraviolet from the transition $(2p)^4 \ ^3P_{2,1,0} - (2p)^3(^4S^0)(3s)^1 \ ^3S_1$. Since this transition involves the ground state (3P) in an allowed transition and is characterized by large oscillator strengths (f-values), it has the potential of providing an excellent means of measuring atomic oxygen. In order to be useful in mesospheric atomic oxygen measurements, the effective resonance scattering cross section should be much larger than that of competing processes. Since the most significant competing processes would be the Rayleigh scattering of the O resonance radiation (along with all other lamp emissions) by all atmospheric atomic and molecular species, a successful measurement of O density $[O]$ would require that the inequality

$$[O]\sigma_O \gg [M]\sigma_R$$

be satisfied. Here σ_O and σ_R are the cross sections for resonant O scattering and Rayleigh scattering, respectively, and $[M]$ is the total number density of atmospheric molecules. If we intend to measure $[O]$ at altitudes of perhaps 74 km where the anticipated $[O] \approx 10^9$ atoms/cm³ and the total atmosphere number density, $[M]$, is in the order of 10^{15} and the effective atomic oxygen resonance cross section, σ_O , is approximately 3.4×10^{-14} cm², then the Rayleigh scattering cross section would need to be less than 10^{-20} cm². At the wavelengths of concern, ≈ 130 nm, σ_R is approximately 3.5×10^{-24} cm².

From the above argument it is apparent that little difficulty should be expected from competing scattering processes at altitudes above 75 km. Since the intervening gas has the potential of absorbing and multiple scattering the return, light absorption in the optical path needs to be considered. Ideally, at the maximum $[O]$ ($\sim 10^{11}$ atoms/cm³)

$$[O]_{\max} \sigma_0 L < 1$$

where L is the total path length in cm. If $L = 100$ cm

$$[O]_{\max} \sigma_0 L = 10^{11} \times 3.42 \times 10^{-14} \times 10^2 = 3.42 \times 10^{-1}$$

It is apparent from the above that the inequality is met but not by such an overwhelming amount that the effects of light beam attenuation can be ignored. It does mean that in all probability multiple scattering and spectral hardening (change in the apparent absorption cross section as a function of path length due to the preferential absorption of the emission line centers) can be neglected without serious error. It is also apparent that the resonance effect is sufficiently strong that at the maximum anticipated density a large fraction (in the order of 1 - 10%) of the resonance photons will suffer a scattering interaction within the reasonable dimensions of a scattering measurement. Furthermore, the return signal to be detected should be large if a reasonably large number of photons can be generated within the optical width of the scattering atoms. One approach would be to excite the resonance lines from a continuum source; however, it is virtually impossible to obtain enough photons within the oxygen absorption bandwidths from any reasonable source to make this approach reasonable. An alternative would be to generate oxygen emissions within a gas discharge containing oxygen. In order to be practical as a measurement tool, the oxygen emissions should be from an optically thin source to prevent the centers of the lines from being re-absorbed before leaving the lamp. Absorption results in reversal or broadening of the emission line shapes. Other factors influencing the shape of the emission lines are Doppler broadening due to the motions of the emitting atoms, pressure broadening due to collisions between the excited atoms and other atoms and molecules, and finally broadening due to collisions with both ions and electrons.

Inasmuch as the best choice for a light source to excite the 0 resonance transitions appears to be the 0 emissions themselves, the generation of these emissions and their interactions with the scatters needs to be investigated in reasonable detail. The energy level diagram showing the transitions pertaining to the oxygen resonance radiation is shown in Figure 1. Although the scale has been distorted for the purpose of illustration, the three ground state $(2p)^4 \ ^3P_{2,1,0}$ energy levels are indicated for $J = 0, 1,$ and 2 . As the atomic oxygen in a resonance lamp is excited, one of the $(2p)^4$ electrons is raised to the $3s$ level $2p^3(^4S^o)3s^1 \ ^3S^o$ corresponding to a wave number of $76,795 \text{ cm}^{-1}$. As this excited electron returns to the ground state it will return to one of the $3p$ levels according to the statistical weights appropriate to the $J = 0, 1, 2$ levels which are respectively 1, 3, and 5. This resultant idealized atomic oxygen emission spectra is shown in Figure 2.

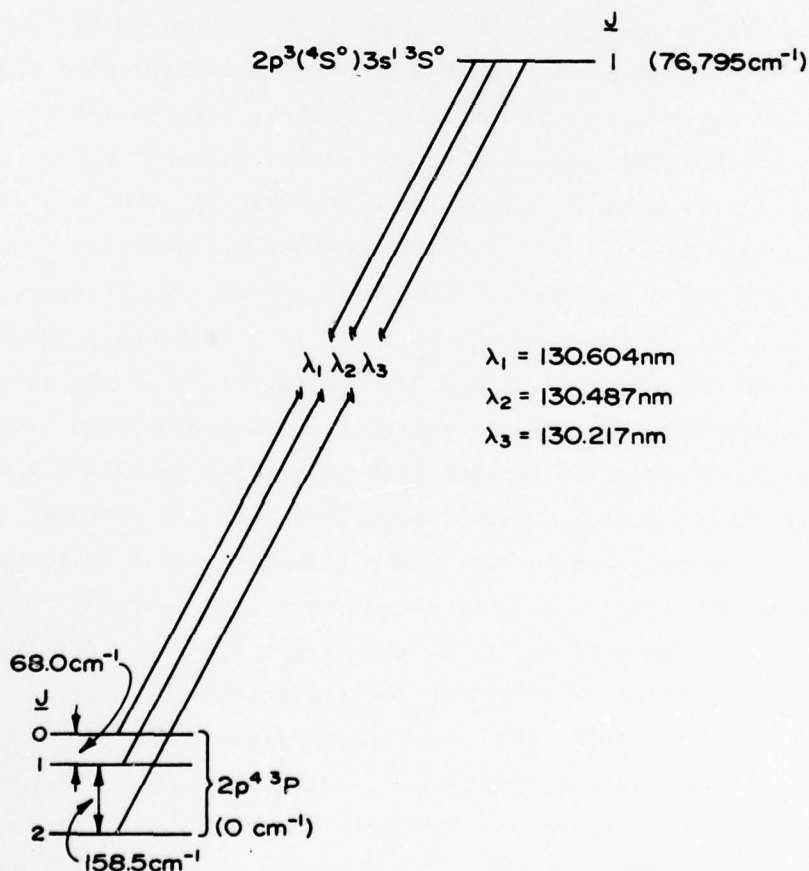


Figure 1. Energy level diagram for atomic oxygen resonance emissions.

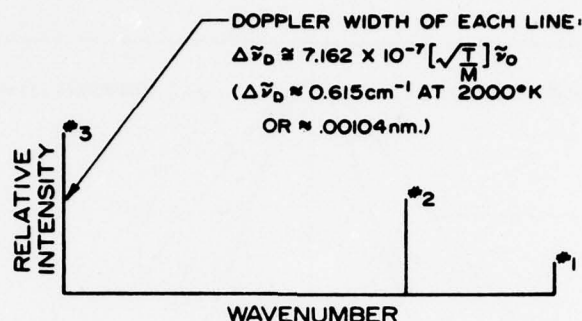


Figure 2. Idealized O triplet emission spectrum with no self-absorption and 5:3:1 line intensity ratios.

The height of each line will follow the ratios 1, 3, and 5 with wavelengths of 130.604, 130.487, and 130.217 nm respectively. Since the emitting atoms will have thermal kinetic energy at the time they emit a photon, the resulting lines will not have their very narrow natural width as indicated, but will be Gaussian shaped with a half width (Doppler width) of

$$\Delta \nu_D = 7.162 \times 10^{-7} (T/M)^{1/2} \nu_0$$

which as a point of reference corresponds to 1.04×10^{-3} nm at a temperature of 2000° K.

The effective cross section or absorption coefficient in the ambient oxygen for each radiation line needs to be considered. These absorption coefficients will be dependent on the oscillator strength (f-number) for the transition, which have been quite well documented from empirical measurements. The absorption coefficient is also dependent on two temperature related effects. For maximum absorption coefficient the emission and absorption line profiles should be identical, which in general they are not, as indicated in Figure 3. Additionally, the absorbing oxygen temperature will alter the population of the three ground state levels from that predicted by the 1, 3, 5 statistical weights. The effective absorption coefficient for each of the three lines will follow the actual population of the three levels.

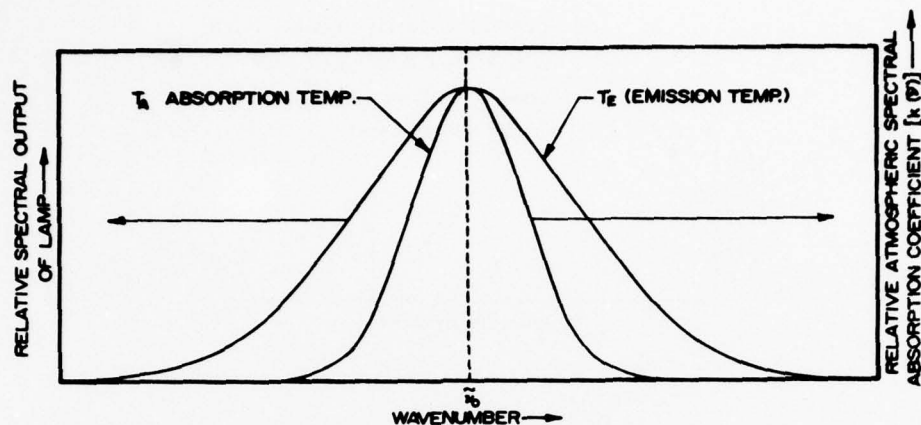


Figure 3. Doppler-broadened low temperature absorption line and higher temperature emission line typical of the conditions anticipated in an atomic oxygen measurement where the lamp emission temperature exceeds the ambient temperature of atmospheric O.

A simple Doppler-Doppler line absorption model yields the following expression for the absorptance, A_α , which is the fractional decrease in intensity of an incident beam. For a single line

$$A_\alpha = \frac{\int_{-\infty}^{+\infty} I(\omega) [1 - \exp(-k_0 \ell e^{-\omega^2})] d\omega}{\int_{-\infty}^{+\infty} I(\omega) d\omega}$$

where $I(\omega) = C e^{-(\omega/\alpha)^2} \equiv$ assumed emission line shape

$$\omega = 2(\nu - \nu_0) / \Delta\nu_D \sqrt{\ln 2}$$

ν = frequency

ν_0 = line-center frequency

$\Delta\nu_D$ = Doppler breadth of the absorption line

α = (emission line breadth)/(absorption line breadth)

$\alpha = (T_E/T_A)^{1/2}$ for the Doppler-Doppler case

T_E = effective temperature of emitters

T_A = effective temperature of absorbers

$k_0 \ell$ = optical depth

k_0 = absorption coefficient at the line center

ℓ = thickness of (uniform) absorber

The expression for A_α may be simplified when $k_0 \ell \ll 1$, i.e., under optically-thin conditions. In this case, the approximate expression for A_α becomes

$$A_\alpha \approx (k_0 \ell) \frac{\int_{-\infty}^{+\infty} e^{-\left(\frac{1+\alpha^2}{\alpha^2}\right)\omega^2} d\omega}{\int_{-\infty}^{+\infty} e^{-(\omega/\alpha)^2} d\omega}$$

$$\approx [k_0 \ell] / \sqrt{1 + \alpha^2} = (k_0 \ell) F(\alpha)$$

$$\text{where } F(\alpha) = (1 + \alpha^2)^{-1/2}.$$

The extension of the Doppler-Doppler line absorption model to the case of the OI multiplet of interest (three simple, non-overlapped lines) is readily made by writing

$$\bar{A} \approx \frac{\sum_{i=1}^3 \int_{-\infty}^{+\infty} I_i(\omega) [1 - \exp(-k_0^{(i)} \ell e^{-\omega^2})] d\omega}{\sum_{i=1}^3 \int_{-\infty}^{+\infty} I_i(\omega) d\omega}$$

where the summation index i corresponds to a particular member of the absorption triplet. When $k_0^{(i)} \ell \ll 1$ for $i = 1, 2, 3$, the above equation reduces to

$$A \approx \ell F(\alpha) k_0^{\text{eff}}$$

where $k_0^{\text{eff}} [= (\sum_{i=1}^3 k_0^{(i)} C_i) / (\sum_{i=1}^3 C_i)]$ is an effective line-center absorption coefficient. The constants C_i characterize the strengths of the emission lines which stand in the relationship 5:3:1 when negligible self-reversal occurs in the source.

The effective line-center absorption coefficient may be written in terms of the line-center coefficient for the strongest absorption line. If we associate $i = (1, 2, 3)$ with the $2p ({}^3P_2, {}^3P_1, {}^3P_0) \rightarrow 3s {}^3S_1$ transitions, respectively, then $i = 1$ will designate this line. The above equation may then be written in the form

$$\begin{aligned}
 k_o^{\text{eff}} &= \left[\frac{5}{9} k_o^{(1)} + \frac{3}{9} k_o^{(2)} + \frac{1}{9} k_o^{(3)} \right] \\
 &= k_o^{(1)} \left[\frac{5}{9} + \frac{3}{9} \frac{k_o^{(2)}}{k_o^{(1)}} + \frac{1}{9} \frac{k_o^{(3)}}{k_o^{(1)}} \right]
 \end{aligned}$$

Since the relative populations of atoms in the three levels of the 3P ground state are given by

$$P_j = \frac{g_j e^{\Delta E_j/kT}}{\sum_i g_i e^{-\Delta E_i/kT}}$$

where $j = 2, 1, 0$ and where the statistical weights g_j are 5, 3, and 1, we can then calculate the ratios $\frac{k_o^{(2)}}{k_o^{(1)}}$ and $\frac{k_o^{(3)}}{k_o^{(1)}}$. The effective overall absorption coefficient, k_o^{eff} , is given by

$$k_o^{\text{eff}} = k_o^{(1)} \left[\frac{5 + 3e^{-228/T_A} + e^{-326/T_A}}{9} \right]$$

where T_A is expressed in $^{\circ}K$.

Since k_o , the line center absorption coefficient, is related to the atomic oscillator strength (f-number) by

$$k_o = \frac{2N\pi e^2 \sqrt{\ln 2} f}{mc \Delta \tilde{\nu}_o \sqrt{\pi}}$$

Using recent measurements of f-number for the oxygen resonance transitions of approximately $f = 0.046$, the effective absorption coefficient for $300^{\circ}K$ scatterers is $1.5 \times 10^{-14} [0] \text{ cm}^{-1}$.

Figure 4 shows the effect of differing emitter-to-absorber temperature ratios on the effective absorption. This particular plot is based on an assumed $1600^{\circ}K$ Doppler emission temperature and absorber temperature between 100 and $500^{\circ}K$.

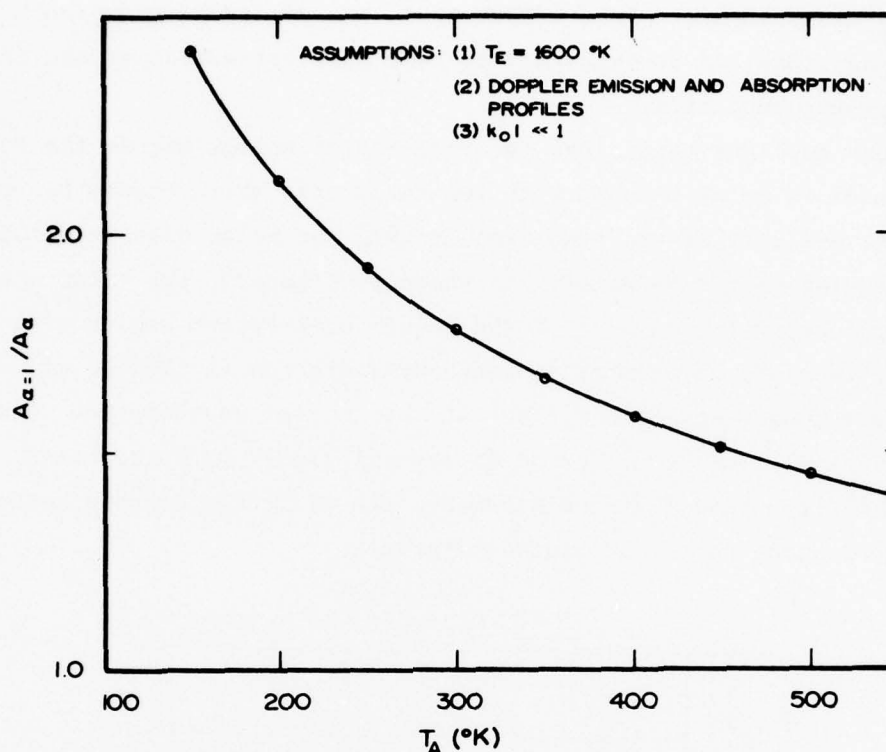


Figure 4. Correction factor resulting from unequal emission and absorption temperatures based on an emission temperature of 1600°K, Doppler line shapes, and negligible self-reversal either inside or outside the lamp.

With the physical basis for using the atomic oxygen resonance emissions for the measurement of atmospheric O density having been established in principle, the remainder of this report will deal with consideration of natural competing background emissions, the hardware required to accomplish an O density measurement, the calibration techniques necessary to obtain an absolute measurement of O density, and finally a discussion of the results from a pair of flights based on the above.

BACKGROUND RADIATION

Any radiation within the field of view of the detector of wavelength within the spectral response and acceptance of the detector will have the effect of adding unwanted background signal to the sought resonantly scattered light signal, or in severe cases may saturate the detector and pre-

vent any measurement. Since measurements are desirable under both day and night conditions, it is necessary to have some estimation of the intensity of background radiation.

Under daylight conditions the majority of energy within the vacuum ultraviolet is solar related with two conditions which should be considered. The first and most severe condition is when the solar disc is within the field of view of the detector. As shown in Figure 5, the solar spectrum within the sensitive portion of the vacuum ultraviolet region of a typical detector consists of primarily blackbody radiation ($\sim 5000^\circ\text{K}$) at wavelengths 140 nm and longer and line spectra at the shorter wavelengths. The dominant line emissions from H, O, C, and Si are all likely to be detected. Wavelengths shorter than 121.6 nm H Lyman- α are of little concern because of the transmission cutoff of window materials.

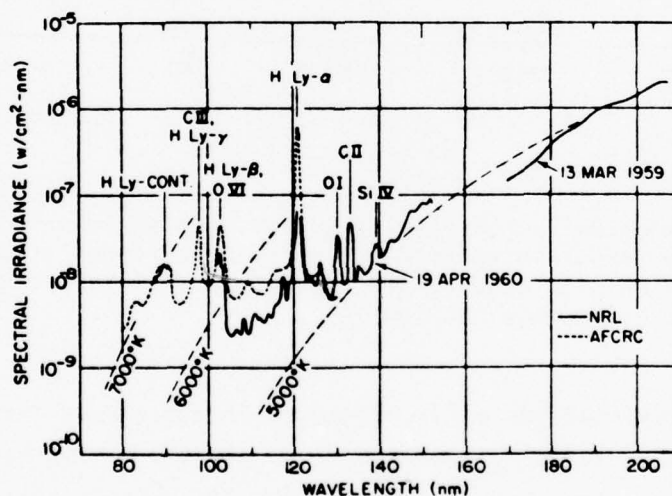


Figure 5. Solar ultraviolet spectral irradiance above the Earth's atmosphere observed with a photographic spectrograph (NRL) and a photoelectric monochromator (AFCRC). The lines are shown with an effective line width of 10 Å. *Reproduced from Naval Research Laboratory data.*

The solar spectrum presented in Figure 5 represents the spectral irradiance above the earth's atmosphere. As the atmosphere is penetrated, both scattering and absorption processes become significant. In particular, the H Lyman- α is strongly scattered and since the O transitions are resonance transitions, these wavelengths are also strongly scattered. Compared to the situation at the top of the atmosphere as the altitude

is reduced, the intensity in the direction of the solar disc would become attenuated while the intensity in all other directions would increase due to scattered light. This situation continues with increasing optical depth until the radiation is isotropic and absorption effects (largely from O_2) decrease the intensity at lower altitudes.

The optical depth of the O transitions approach unity at an altitude of about 650 km and at an altitude of 100 km is well over 10^4 [Strickland and Donahue, 1970]. It is therefore safe to say that the O radiation is isotropic at the altitudes in which our O measurements would be made. The measured O height profile O resonance radiation due to solar UV is shown in Figure 6.

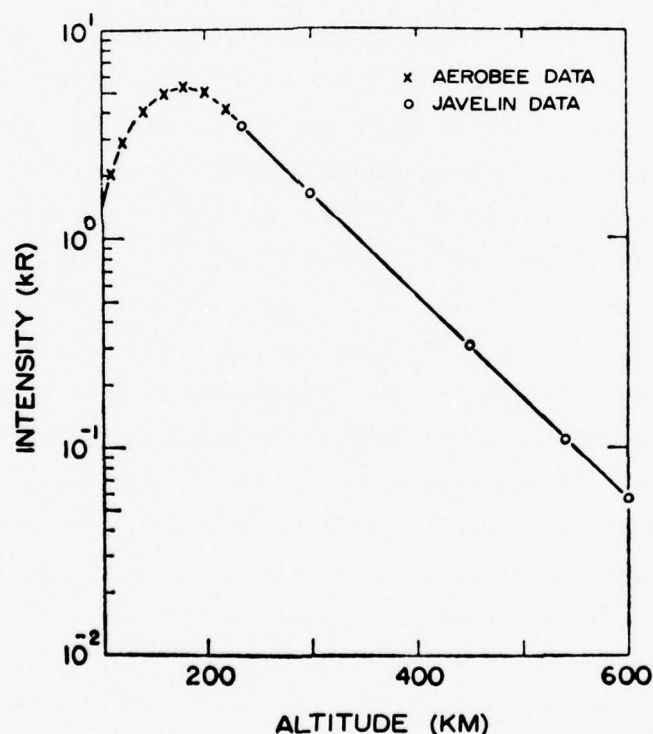


Figure 6. Smoothed experimental 1304 intensity height profile including the low tube data of *Fastie et al.* [1964] and high altitude data of *Fastie* [1968].

It might be expected that the other UV emission lines and continuum radiation would be scattered (Rayleigh), but not nearly to the extent of a line involving a resonance transition. This means that a constant Rayleigh scattered light background independent of direction and a high intensity source in the direction of the solar disc may be expected. In

all probability, the O measurement at higher altitudes (above 100 km) with the detector looking at the sun would be difficult, but in other directions could be made without great difficulty. As the altitude is decreased, the measurement becomes more difficult.

The night background radiation is, of course, lacking the direct solar radiation but has considerable scattered radiation. Scattered hydrogen Lyman- α , for example, has about the same intensity relationship between day and night as does bright direct light and a cloudy day. In addition to the prominent H Lyman- α emissions, the O resonance radiation triplet, an O emission ($3P - 5S^0$) at 135.6 - 135.9 nm and N₂ band emission all contribute to the background radiation. Although the airglow is a function of altitude, latitude, and other geophysical conditions, all of the non H Lyman- α radiations account for only a few hundred Rayleighs of background [Hicks and Chubb, 1970; Peek, 1970]. The H Lyman- α emissions are on the order of less than one to several kilo Rayleighs.

The implications of the above considerations in terms of an anticipated count rate for a typical detector having a geometric factor (detector area \times solid field of view angle) of $1.7 \times 10^{-2} \text{ cm}^2 \text{ sr}$ and an effective quantum efficiency of 1×10^{-4} over the spectral region of interest is a count rate of ~ 25 counts/sec as compared with $\sim 10^3$ counts/sec for O density $\sim 10^{11}/\text{cm}^3$. This background rate is significant but tolerable. It should be noted that the intensity of the night airglow is a function of altitude because of absorption processes at the lower altitudes. The emission profile of H Lyman- α and other prominent lines are shown as functions of altitude in Figure 7. Although these measurements were under auroral conditions, the emission was believed to be of non-auroral origin, i.e., resonantly scattered solar emissions; and would be, therefore, somewhat typical of the undisturbed atmosphere as well. Similar behavior may be expected from all vacuum ultraviolet emissions.

ATOMIC OXYGEN RESONANCE LAMP

The atomic oxygen resonance lamp would ideally produce high intensity emissions at 130.2, 130.4, and 130.6 nm having theoretically predicted amplitude ratios 1, 3, and 5. An emission temperature of the lamp approximately equal to the anticipated atmospheric O temperature would be

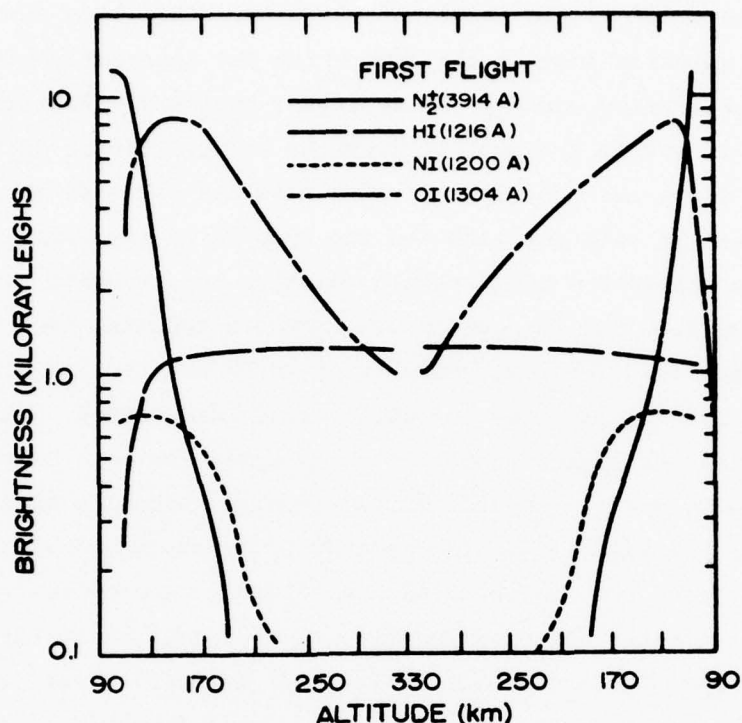


Figure 7. Measured altitude profiles of prominent emissions from N_2 , H, N, and O [Peek, 1970].

desirable from the standpoint of maximum effective absorption cross section; however, this condition produces scattering that is relatively sensitive to atmospheric temperature variations which would then need to be known. If the resonance emission temperature were quite hot in comparison to the atmospheric temperature, then atmospheric temperature would be of little consequence in the scattering process. The effective cross section would be considerably reduced, however.

Similarly, there is a compromise between the lamp intensity and self-absorption producing non-gaussian emission line shapes which can introduce considerable error into the predicted absorption cross sections. If the O concentration in the lamp is low and the total pressure in the lamp (O, O_2 and any other carrier gas) is low, then the emission lines have a pure Doppler shape but low intensity. If the O partial pressure becomes too large, then a portion of the generated photons will be absorbed before they can get out of the lamp. As might be expected, those photons having wavelengths near the line center are more likely to be

absorbed than those in the skirts of the line. This self-absorption results in an emission leaving the lamp which has abnormally wide skirts and a suppressed line center. An indicator that self-absorption is becoming significant is a departure from the 1, 3, 5 line height ratios. This occurs since the most intense line also has the most absorbing atoms between the emitting atom and the outside of the lamp, thus increasing its absorption coefficients relative to the other lines.

The lamp selected for use in measurements reported here was developed by Xonics. The lamp consists of an RF excited low pressure discharge in a flowing fill gas of inert carrier and oxygen. The entire lamp including the oxygen supply is permanently sealed. Molecular oxygen is generated in one of the arms of the lamp by heating a small quantity of an oxygen-bearing solid. The heating is accomplished by a small temperature regulated furnace which may be adjusted to produce the proper oxygen release rate. This oxygen flows into a coaxial cavity having a center electrode excited by high voltage RF exciter at approximately 180 MHz. The resulting discharge which occurs primarily in a few Torr pressure of inert gas dissociates the molecular oxygen and excites the atomic oxygen resonance lines. The end of the coaxial discharge chamber is sealed with a CaF_2 window transparent to the resonance radiation but largely opaque to hydrogen Lyman-alpha radiation (121.6 nm) which is difficult to avoid in any discharge lamp. The oxygen is removed from the discharge chamber by a chemical getter active for oxygen but inert to the carrier gas. This getter is located in a second arm attached to the discharge chamber. With the combined operation of the oven controlled oxygen generator and the getter, a dynamic equilibrium is established with oxygen flowing through the discharge chamber at a relatively constant and controllable partial pressure.

As with any equilibrium condition a transient condition exists as the process is started. In the case of the oxygen resonance lamp, the lamp has insufficient oxygen at start-up due to the continued action of the getter, but with virtually no oxygen being supplied with the oven off. The typical start-up transient in terms of oxygen triplet intensity is shown in Figure 8. The initial increase in intensity after start-up has a time constant of approximately 15 minutes which varies somewhat from one lamp to the next. To allow time for stabilization, the oxygen lamp

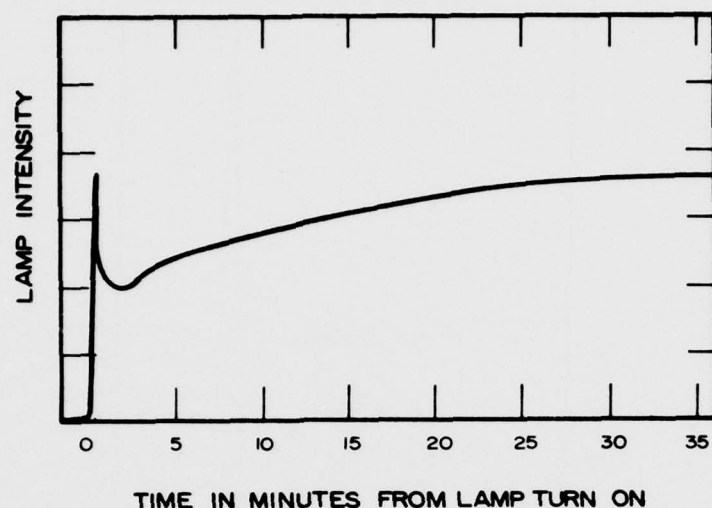


Figure 8. Typical start-up transient in an Xonics 0 resonance lamp. The intensity is the total emission from all three resonance lines. The lamp has been operated and then turned off for several hours before starting this measurement. The character of the start-up transient has been found to be a function of this operating history.

must be on continuously for at least a half hour before flight. In addition to the start-up transient, there is a slow decay in the lamp intensity with cumulative operating time. This slow deterioration appears to have a time constant of typically 100 hours. Because of the cost of lamps, and the required time and effort involved, this deterioration has not been studied in any detail. It is unknown how uniformly the lamps deteriorate or how the line shapes, as evidenced by line height ratios and doppler widths, vary during the aging process.

As indicated previously, the line height ratios provide an indication of the amount of self-absorption taking place and high intensity and freedom from self-reversal are mutually exclusive. The compromise arrived at for the lamps flown at White Sands is shown in the typical spectrum in Figure 9. The line height ratios are approximately 1, 2.7, and 4.3 with an on axis intensity of 7×10^{12} photons (sec sr) $^{-1}$ from all three lines together.

Since the emitting volume of the lamp is cylindrical and has a length to diameter ratio of in the order of 3:1, it may be anticipated

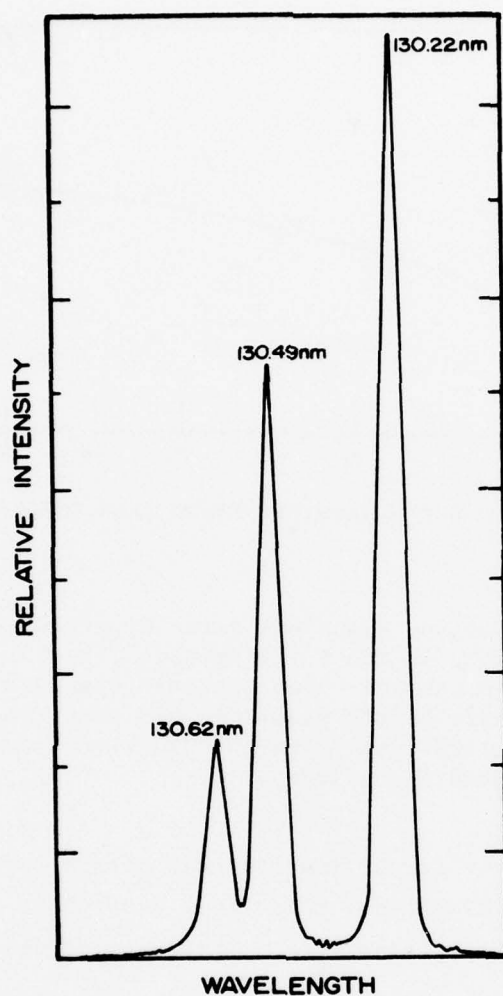


Figure 9. Measured lamp spectrum for a lamp typical of those flown for 0 measurements. The indicated line widths represent the resolution of the spectrometer not the lamp. The line height ratios are approximately 4.3:2.7:1.

that the off-axis intensity would drop rather significantly. As shown on the measurement in Figure 10, this is indeed the case. One might also anticipate that the degree of self-absorption would also vary with the off-axis angle since the emissions from deep within the lamp would be blocked. This effect has not been measured.

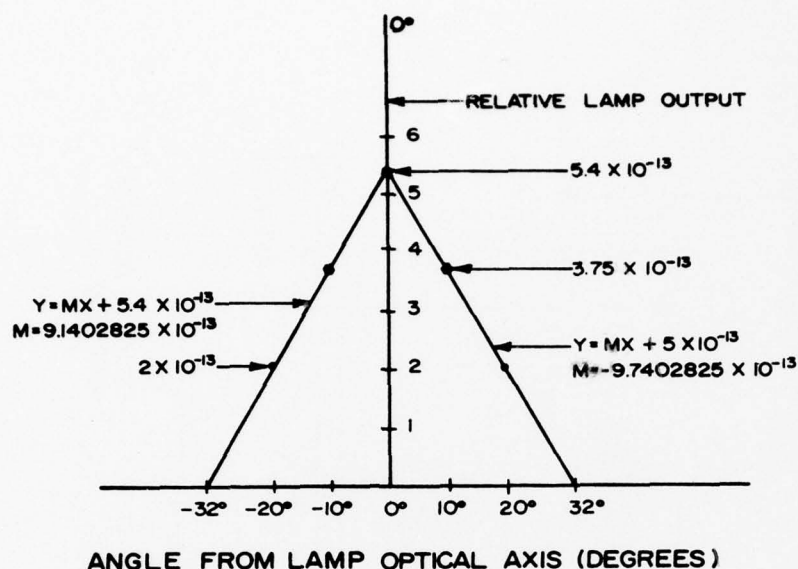


Figure 10. Measured lamp intensity 0 emissions from an Xonics resonance lamp as a function angle from lamp optical axis.

The block diagram shown in Figure 11 shows the elements involved in the resonance lamp system. In addition to the oven controller previously mentioned, the lamp system has an intensity monitor based on a photo transistor sensitive to visible oxygen emissions and a controllable RF oscillator-amplifier to drive the lamp. The lamp oven controller, in addition to providing the means of maintaining the oven at a fixed temperature, also provides monitors of both the heater voltage and lamp oven temperature. These monitors are only relative and therefore do not aid greatly in an absolute calibration. The RF oscillator may be externally driven with a square wave for the purpose of turning the oscillator on and off to modulate the lamp with the desired frequency (0 - 1 kHz capability) and duty factor.

A photo transistor sensitive in the visible and near IR is used to provide a monitor of lamp intensity. Unfortunately, the transistor was sensitive to too much radiation other than that relating to oxygen resonance emissions and was both temperature sensitive and sensitive to ambient light entering the lamp. In the practical sense it could only be relied upon to determine if the lamp was on or off.

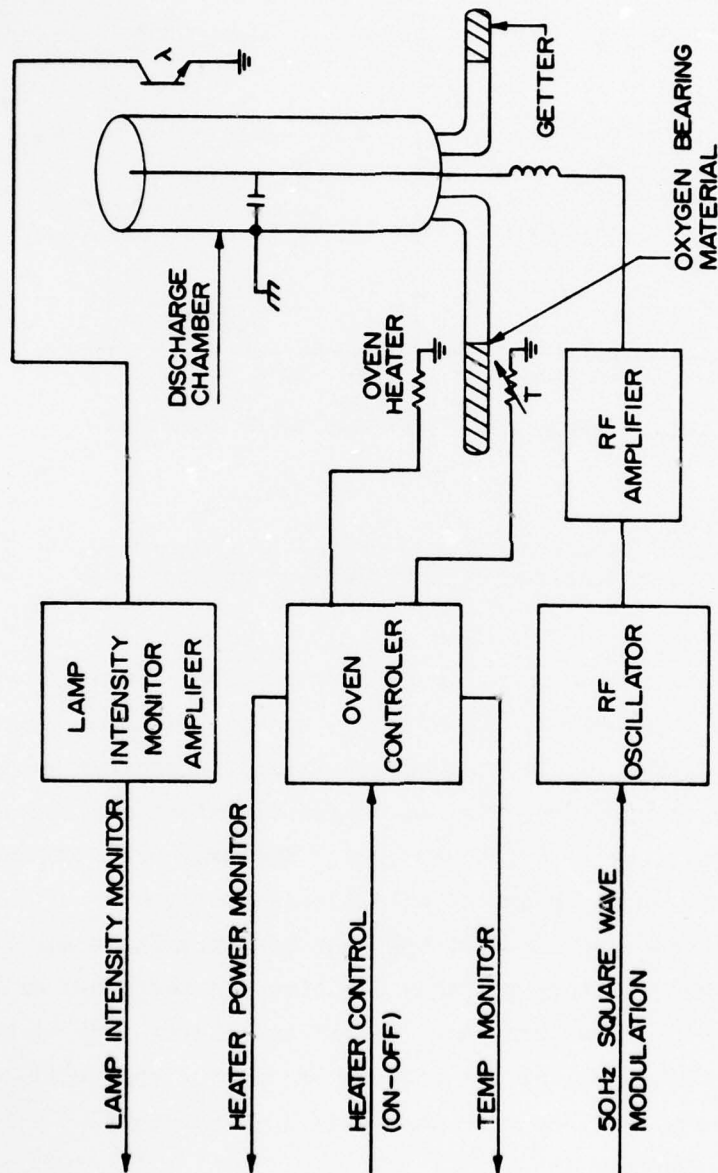


Figure 11. Resonance lamp system including lamp control, excitation, and monitoring process.

Measurement of the optical width of the lines due to Doppler broadening has been carried out on Xonics and other very similar lamps using an Echelle spectrometer having a resolution of 4 mÅ [Xonics, *private communication*]. After deconvolving the measured line width with the instrument resolution, it appears that the emission temperature is in the order of 1600°K. It should be pointed out that actual measurements were not taken on the lamps which were flown and the assumption that the measured lamps and the flown lamps are the same (in terms of 0 pressure and RF excitation levels, etc.) must be made for want of better measurements. A knowledge of instrument response as a function of rocket attitude and velocity has produced evidence that the assumption of a 1600°K emission temperature is not inconsistent with the data.

DETECTORS

Inasmuch as the function of the detector system is to transform the scattered photon flux into a measurable electrical quantity (pulses, voltage or current), the ideal detector would have high sensitivity to only the resonance radiation while rejecting all other radiation sources. It would be physically small to allow good definition of its field of view and would have very wide dynamic range with complete linearity. Obviously such a detector cannot be realized in the real world, but the above criteria serve as a basis of judgment for the several possible detectors which might be used.

Possible classes of detectors include solar blind photomultipliers, geiger tubes, and curved channel electron multipliers. All of the above devices are most naturally photon detectors as opposed to DC detectors, i.e., a single photon could result in the production of an electrical pulse which could be counted. The photomultiplier, and to a smaller extent the channel electron multiplier, can also be used in the DC current mode where the measured current is related to a time average of the detected photon flux. Although the photomultiplier and channel electron multiplier can be used in either mode, their linearity over wide ranges of input photon flux rates is substantially better in the photon counting mode. These devices will therefore only be considered as photon detectors.

Geiger Tubes

A Geiger tube is a gas-filled detector which can be designed for the detection of vacuum ultraviolet photons. It relies on photoelectric ionization within an appropriate filling gas. The free electron is accelerated toward a very thin wire anode by the field established by the tube operating voltage. When the electron reaches a point near the wire where the field gradient is sufficient to allow the electron to achieve sufficient kinetic energy between collisions to produce ionization, a Townsend avalanche is initiated. The discharge is terminated by a number of mechanisms including a drop in the anode voltage, expansion of the positive ion sheath from around the anode altering the potential gradient, and energy absorption in dissociating quenching gas molecules in favor of continued ionization.

As a first order approximation, the spectral response of a Geiger tube will be the combination of the photoionization yield for a filling gas and the transmission of the entrance window. Possible filling gases and their ionization potentials are listed in Table 1.

Table 1
IONIZATION POTENTIALS FOR GEIGER FILLING GASES

Substance	Ionization Potential	
	ev	nm
H _e	24.58	50.43
Ne	21.56	57.49
Ar	15.76	78.67
I ₂	9.28	133.6
NO (Nitric Oxide)	9.25	134.0
C ₆ H ₆ (Benzene)	9.25	134.0
CH ₃ NH ₂ (Methyl amine)	8.97	138.2
C ₂ H ₅ NH ₂ (Ethyl amine)	8.86	140.0

If a filling gas is chosen which has an ionization potential near but below the energy carried by the oxygen triplet, then the detector should be virtually blind to all wavelengths longer than the cutoff. This is very desirable in that it could all but eliminate difficulty from atmospheric emissions, scatterings, and other sources of radiation in the mesosphere.

Unfortunately, not all gases are usable in a Geiger tube. The filling gas must not easily form negative ions or the photoelectrons may be lost before they have a chance to initiate an avalanche and be counted. Furthermore, the gas should have an optical depth as determined by its cross section and pressure chosen to produce high probability of interaction within a short distance of the anode wire. In many cases it is necessary to add an inert (chemically and optically) gas such as Ne to improve the Geiger tube characteristics. Tubes have been made using such combinations as 3% NO and 97% Ne. The stability of such tubes has been relatively poor, presumably due to such effects as dissociation of NO forming N and O and ultimately NO₂ and N₂. The alteration of species within the counter then leads to unstable performance [Samson, 1967].

The short wavelength cutoff of the geiger tube is established in general by the transmission cutoff of the entrance window. Within the portion of the spectrum in which the oxygen resonance triplet exists, there are very few choices of materials which are transparent. Three of these materials are LiF, CaF₂ and MgF₂ with typical transmission curves as shown in Figure 12. CaF₂ has the useful property of having a cutoff wavelength that is noticeably temperature sensitive. At elevated temperatures CaF₂ is relatively opaque to hydrogen Lyman- α at 121.6 nm. This can be usefully applied to reject the substantial Lyman- α intensities found in both the day and night skies.

Further design considerations are indicated in the cross sectional drawing of a Geiger tube shown in Figure 13. This tube is shown with a fine wire (3-4 mil diam) anode positioned a short distance behind the entrance window. Only in the close vicinity of the thin wire is the potential gradient steep enough to allow an avalanche to take place. This is labeled the electron multiplication region. Surrounding this multiplication region is an active volume in which a photoelectron will have a high probability of drifting into the multiplication region before loss by attachment. Outside the active volume the probability of a photoelectron initiating an avalanche is low. Since the energy of oxygen resonance radiation is capable of producing photoelectrons from any metal or other material from which a Geiger tube may be manufactured, the tube will be sensitive to the radiation if the active volume extends to the outer walls. Photoelectrons from the walls can result in sub-

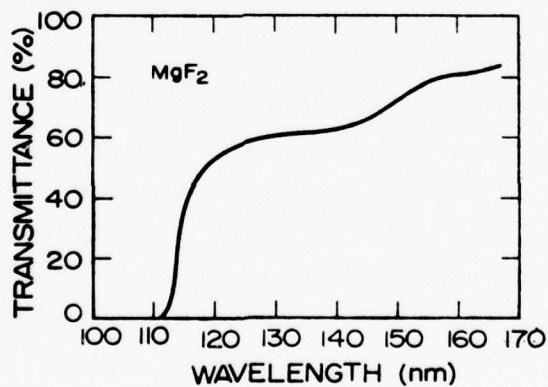
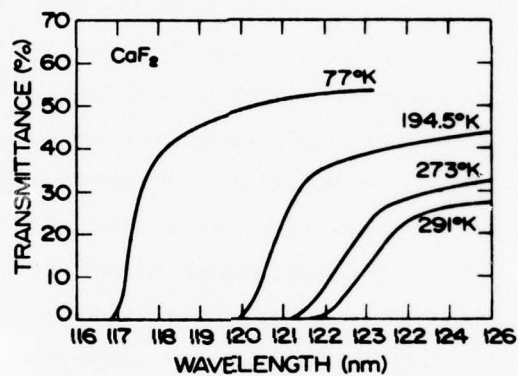
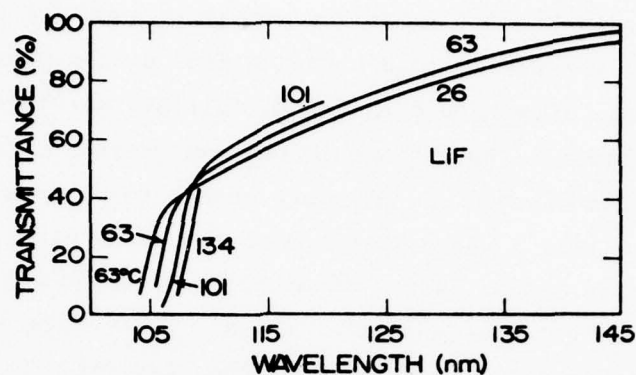


Figure 12. Transmittance of various window materials for use in the VUV with CaF_2 and LiF being shown as functions of temperature [Samson, 1967].

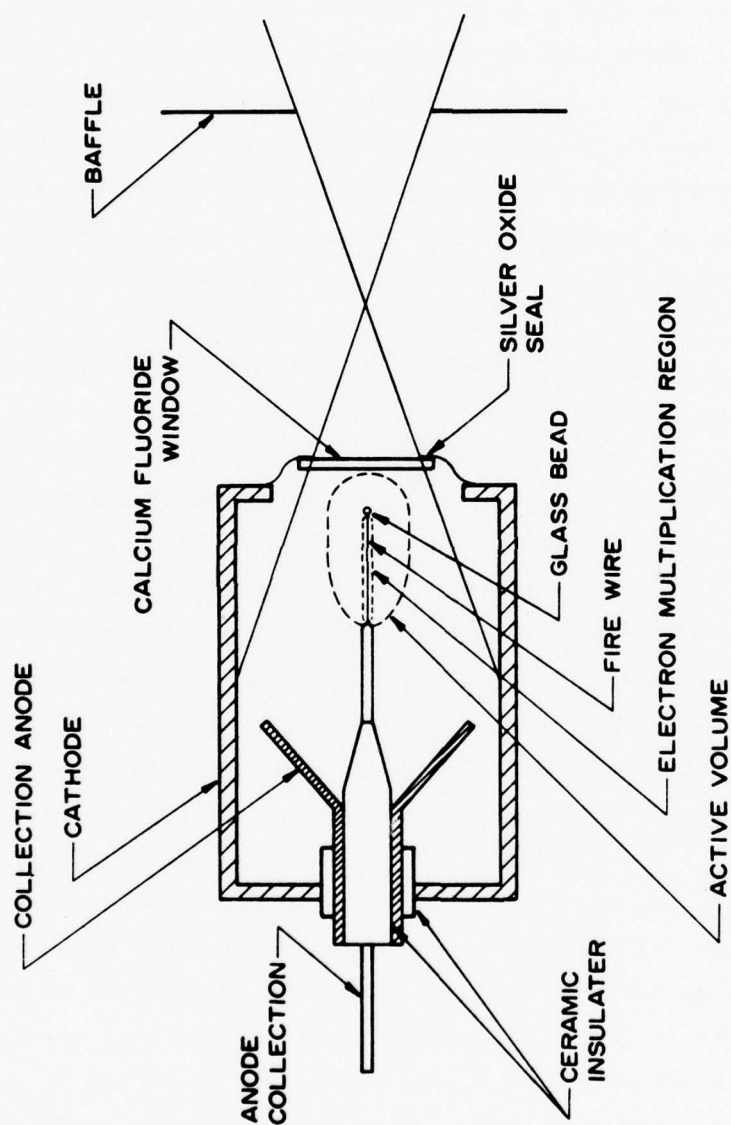


Figure 13. Cross section of a Geiger tube designed for high sensitivity to 0 resonance radiation while having very low sensitivities to both longer and shorter wavelengths.

stantial sensitivity almost all of the way to the visible spectrum. Such sensitivity would be disastrous to an atomic oxygen measurement.

The tube shown in Figure 13 is designed to minimize the likelihood of photoelectrons from the walls being able to produce avalanches. The philosophy is to keep the active volume removed from all materials not at anode potential. Where this is not possible, an auxiliary collection anode is inserted to cause any photoelectrons produced on the walls to be attracted to the collection anode as opposed to the active volume. The collection anode would have large radius surfaces to prevent avalanche to the collection anode. Any photoelectrons released from a material at anode potential cannot be accelerated and thus will not produce an avalanche.

It is necessary to limit the field of view of the Geiger tube using an external baffle to prevent the generation of photoelectrons from portions of the wall not easily collected by the auxiliary anode.

In order to provide an accurate measurement with good spatial resolution on a rapidly moving vehicle like a sounding rocket, the detector count rate needs to be high. A minimum of 100 counts per space or time interval would be considered necessary for 10% statistical accuracy. The detectors need to handle count rates of up to 10^6 counts/second to meet both dynamic range and accuracy requirements for a one second resolving time (≈ 1 km spatial resolution). A Geiger tube is poorly suited to meet these requirements. As shown in Figure 14, the time immediately following an avalanche the potential gradient near the anode wire is reduced because of reduced anode voltage, and because of the presence of a positive ion sheath. Avalanches which should be produced by photoelectrons during this time are drastically modified. For a period of time after the initial avalanche the field gradient is so low that no other avalanches can be initiated. This is defined as the dead time of the tube. After the dead time is a period of time in which the avalanche amplitude will be reduced although photoelectrons may still be counted with appropriately sensitive electronics. This time is the recovery time of the tube. Because of these effects, Geiger tubes can rarely be used at count rates exceeding 10^4 counts/second with rates of $2-3 \times 10^3$ counts/second being more typical of maximum operating points without severe corrections being applied to the data to account for dead time.

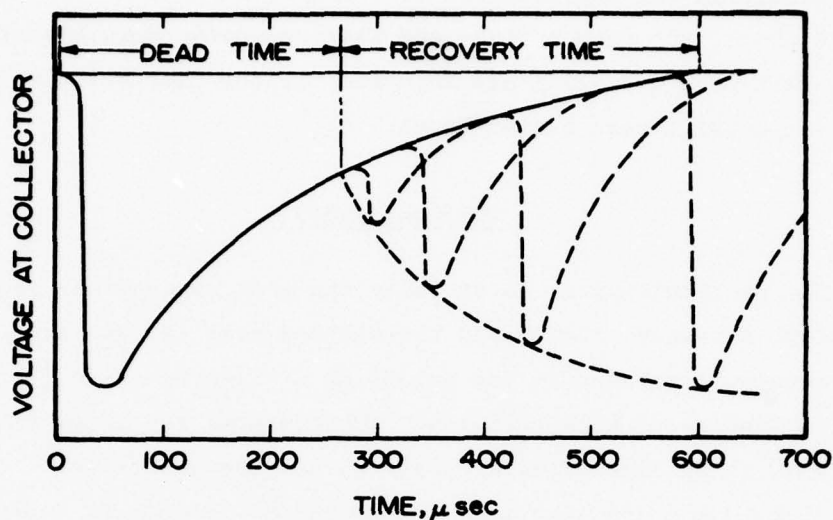


Figure 14. The recovery characteristics of a Geiger tube showing as a function of time from a proceeding count the period of time in which no additional count may be initiated, and the period of time in which a count may be initiated but which has a lower amplitude.

The minimum count rate which might be expected in the mesosphere is in the order of 1 count/second due to cosmic radiation.

In order to achieve a usable accuracy and dynamic range with Geiger detectors, it would be necessary to use at least two detectors having geometric factors (detector area \times solid field of view angle) differing by a ratio of perhaps 100.

In evaluating the Geiger tube detector approach in comparison to other alternatives, it appears that Geiger tubes have excellent potential for high sensitivity (high quantum efficiency) and unequalled ability to reject photons of both short and long wavelengths. It must be emphasized that the sensitivity to protons within the 2,000 to 4,000 Å region must be many orders of magnitude down from that at the oxygen resonance line. Whether this degree of blindness can be achieved is very much in question. The development work has not been done here and no manufacturer could be found that could provide assurance of sufficient solar blindness without the time and expense of development. The dynamic range is comparatively

poor requiring the complication of multiple detectors. In consideration of the above, the fairly risky and time consuming development of a technique with good potential was rejected for the time being in favor of techniques which were better known.

Photomultipliers

The photomultiplier is probably the most extensively used photon detector, not only through the visible and near IR, but also well into the vacuum ultraviolet to the cutoff of Lithium Fluoride (~ 105.0 nm). Its combination of high efficiency photocathode and large electronic gain make it an exceptionally powerful and useful device.

Under ideal circumstances the spectral response of a photomultiplier which might be used for the detection of oxygen resonance radiation would be determined by the combination of the short wavelength cutoff of the entrance window (as discussed previously for the Geiger tube) and the spectral response of the photocathode material. The most commonly used photocathode materials are the alkali halides and, in particular, CsI and KBr. The response of these materials is shown in Figure 15. When combined with a lithium fluoride window, the published (EMR) response characteristics of typical tubes are shown in Figure 16.

As may be noted by a comparison of Figure 16 with Figure 15, the spectral response starts leveling off slightly in the vicinity of 10^{-7} quantum efficiency. This is somewhat unexpected from the response of the photocathode itself. As shown in Figure 17 which shows the quantum efficiency for a number of materials which might be found in a photomultiplier, nearly all materials have a significant quantum efficiency. Inasmuch as the photomultiplier envelope and internal structure, particularly the first dynode, may receive a significant flux of photons resulting in unpredictable response in the mid-ultraviolet where extremely low response is very critical. Measured quantum efficiency in the mid-UV is typically in the order of $10^{-6}\%$.

The photomultiplier is without doubt the fastest responding and widest dynamic range detection device of any to be considered. Photon counting rates well beyond 10^6 /sec are obtainable without difficulty. The quantum efficiency is also at least as high as any of the other de-

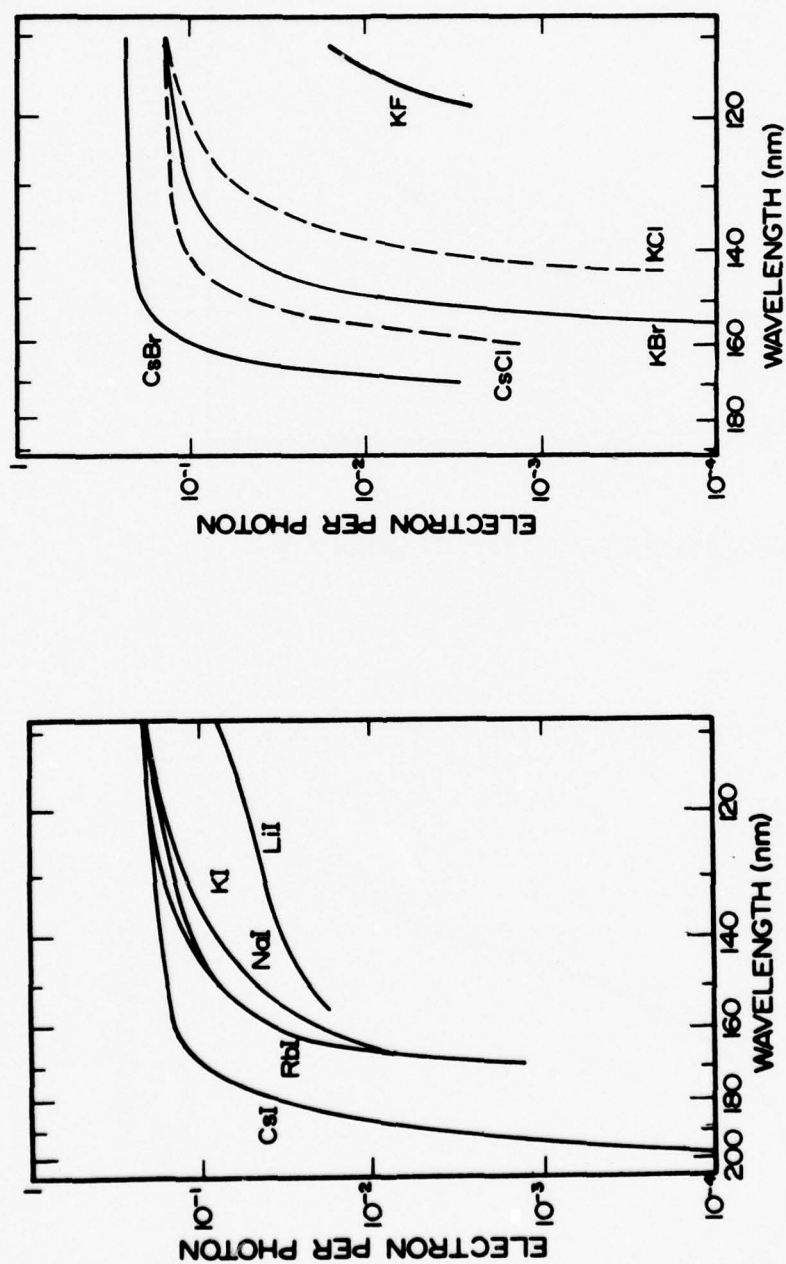


Figure 15. Spectral response of various alkali halide photocathode materials in the vacuum ultraviolet.

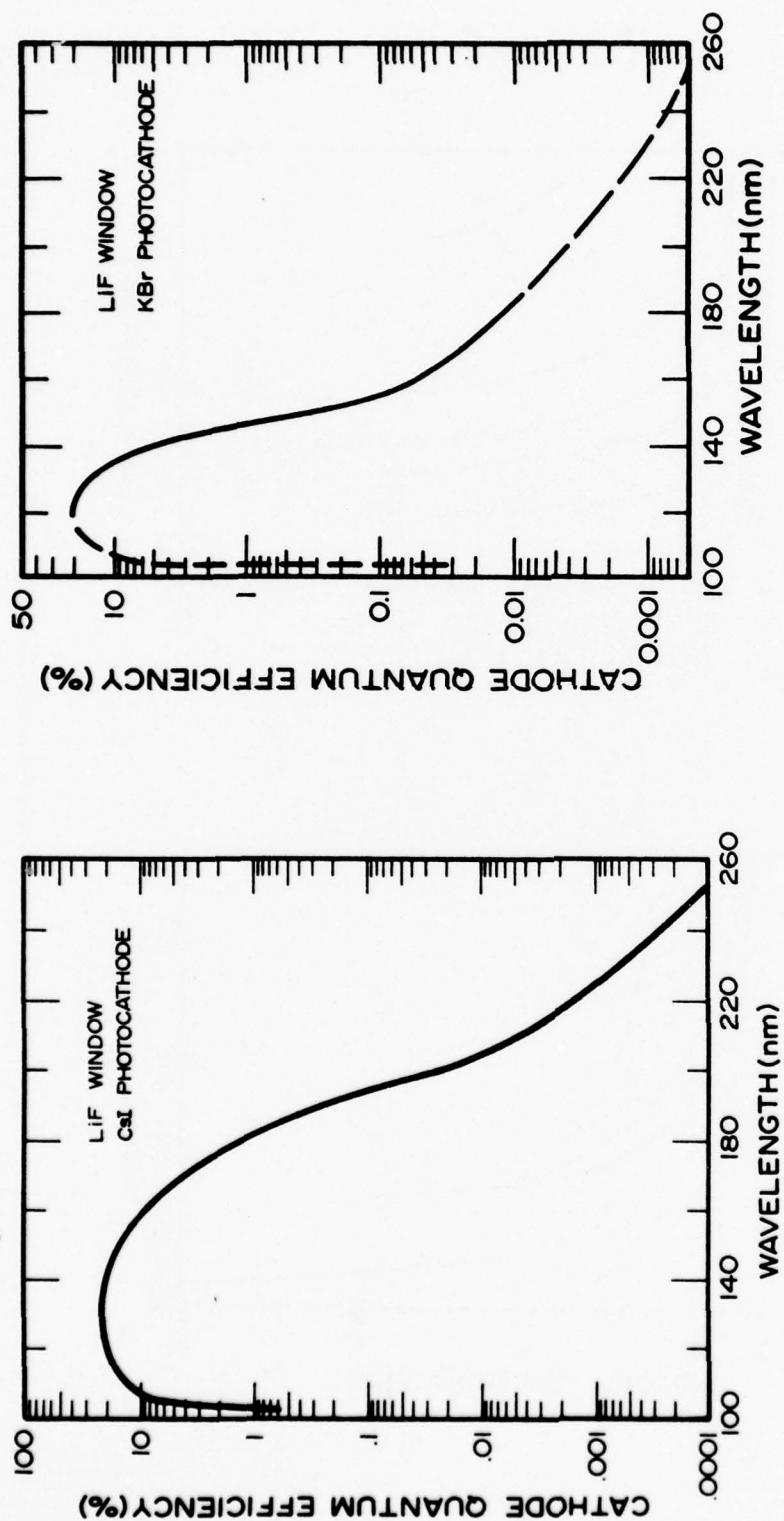


Figure 16. Overall photomultiplier response published by EMR for solar blind photomultipliers. Both response curves are for LiF windows with CsI on the left figure and KBr on the right. The CsI tube has a semi-transparent photocathode while the KBr is on a reflecting substrate.

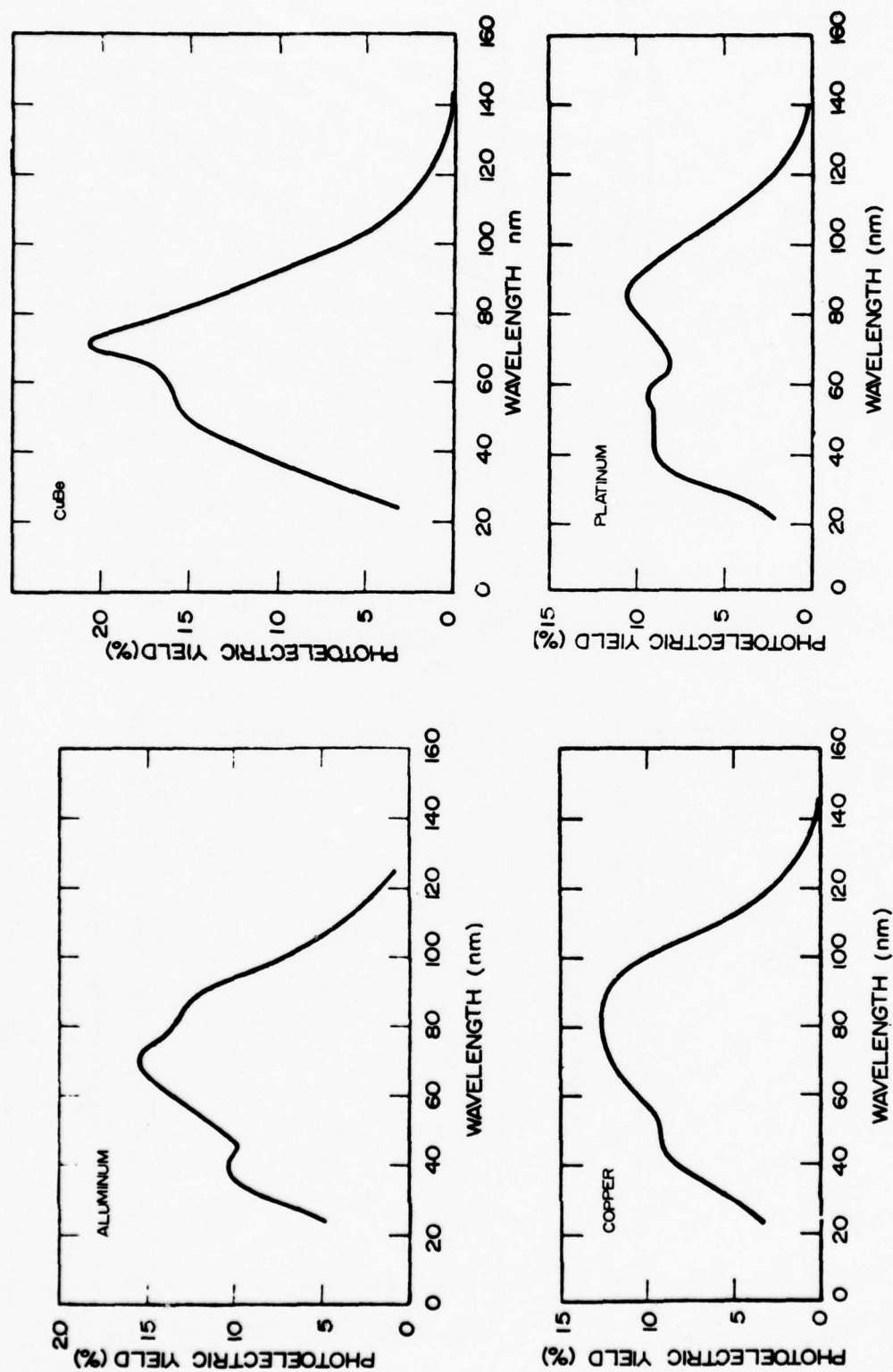


Figure 17(a). Photoelectric yields of various materials likely to be found in photomultipliers as a function of wavelength with normal incidence [Samson, 1967].

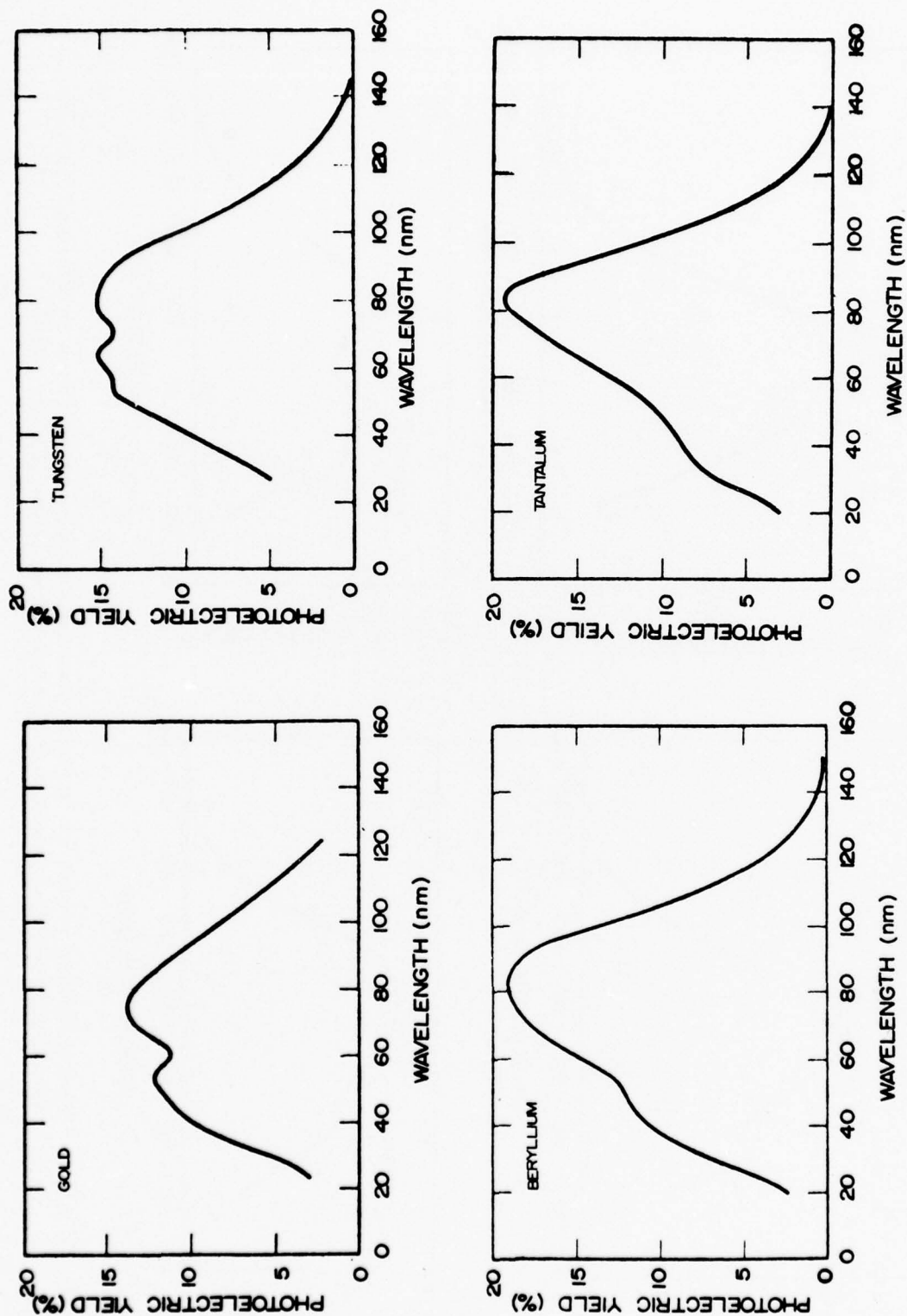


Figure 17(b). Photoelectric yields of various materials likely to be found in photomultipliers as a function of wavelength with normal incidence.

vices and in most cases higher. Its response to the mid-UV is significant and not readily controlled or predicted. The phototubes meeting the selection criterion are also costly and with unpredictable delivery (if available at all). These uncertainties led to the rejection of a photomultiplier as the detector for the atomic oxygen system.

Curved Channel Electron Multipliers

The curved channel electron multiplier (CEM) is based on a simple curved capillary glass tube coated internally with a semiconducting material which serves as a continuous dynode replacing the complex multiple dynode structure of conventional electron multipliers and photomultipliers. The CEM has in addition to very high gain ($\approx 10^8$) a very low background count rate. The CEM is sensitive to electrons and ions with nearly 100% efficiency. It is also sensitive to vacuum ultraviolet radiation between .2 nm and 150 nm. The published quantum efficiency shown in Figure 18 indicates that the CEM would have slightly less than 1% quantum efficiency at the oxygen resonance wavelengths. The short wavelength efficiency which continues to climb with decreasing wavelength could be effectively limited to the cutoff of whatever entrance window material was selected. As indicated previously, heated calcium fluoride would be a good choice inasmuch as it has good transmission at the 0 wavelengths, but is nearly opaque at 121.6 nm. The relatively rapid and continuous quantum efficiency decline at longer wavelengths is valuable in decreasing the effects from undesired atmospheric and solar emissions.

The CEM has relatively good dynamic range capability as shown in Figure 19 in that it is capable of counting at rates in excess of 10^5 counts/sec before the pulse height drops significantly. With sufficiently low electronic pulse height discrimination levels, count rates up to 10^6 per second are possible. Inasmuch as both the maximum count rate and the dark count rate are reduced by about the same factor from those of a solar blind photomultiplier, both the CEM and photomultiplier have about the same dynamic range. The photomultiplier will have somewhat better statistical accuracy owing to the smaller normalized standard deviation obtainable with the photomultiplier's higher count rates.

Inasmuch as the CEM requires hard vacuum (10^{-5} Torr or less) for proper operation and such pressures do not exist in the lower mesosphere,

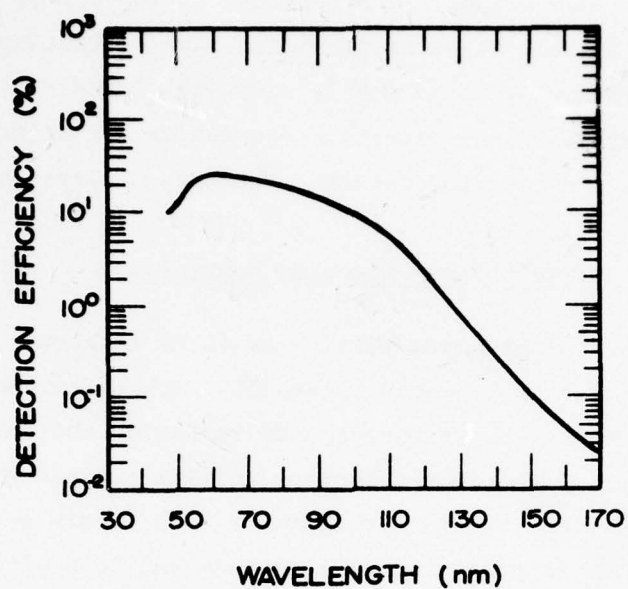


Figure 18. Manufacturer's published CEM quantum efficiency in the vacuum ultraviolet.

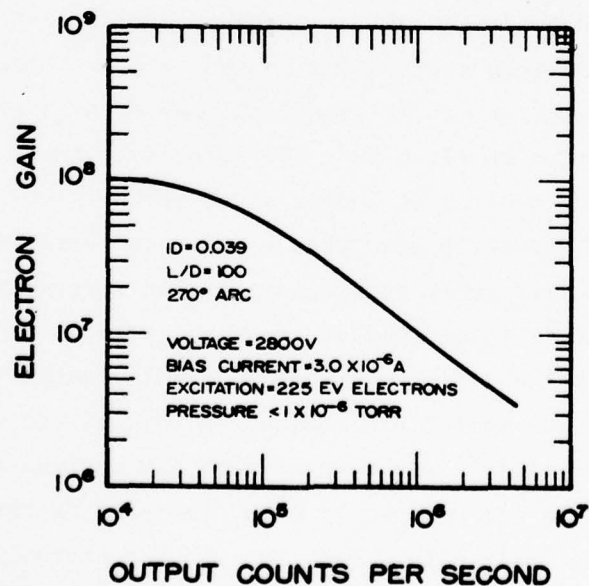


Figure 19. Manufacturer's published CEM gain as a function of count rate.

it is necessary to mount the CEM in a permanently sealed evacuated envelope. In order to maintain hard vacuum, gettering will be required which is a significant complication in what would otherwise be a relatively simple and straightforward detector.

Since the "photocathode" of the CEM is an integral part of the device and is in reality also a distributed dynode, there are some unique capabilities which may result in very low response to mid-UV and visible. The photoemissive dynode material (a high lead content glass) appears unlikely to have any significant emission in the mid-UV and visible. Furthermore, the input to the CEM may be biased negatively with respect to the vacuum tight envelope and all other internal components so that photoelectrons from these areas would be very unlikely to enter the CEM and produce counts. In this manner the overall spectral response of the CEM will be due only to the photoemissive material.

The CEM is comparatively small, light, and only moderately expensive. Although the CEM will require a gettered envelope which is an additional complication, a pressure-tight housing would also be required to prevent difficulties with exposed high voltages on both geiger tubes and photomultipliers. For these reasons the CEM was selected as the detector to be used for the atomic oxygen measurement.

CEM Detector Design

The CEM chosen for the O detector was a Galileo Electro-Optics Model 4013. This multiplier is bent in a 270° segment of a circle with an outside diameter of 1.8 inches. The input is flaired into a funnel having an outside diameter of .15 inches. As shown in Figure 20, the CEM is mounted in a stainless steel housing with a high voltage feedthrough from a pressurized compartment housing a high voltage DC-DC converter. The feedthrough comes through the center of the CEM and also provides a mounting surface for the CEM. The CEM is mounted on a teflon washer since the outside of the CEM has the same semiconductive coating as the inside and mounting to a conductive surface is prohibited. The position of the CEM on the teflon washer is determined by three teflon insulated spring clips.

Since a good vacuum environment is absolutely necessary for proper CEM operation, considerable care is exercised in the assembly to avoid

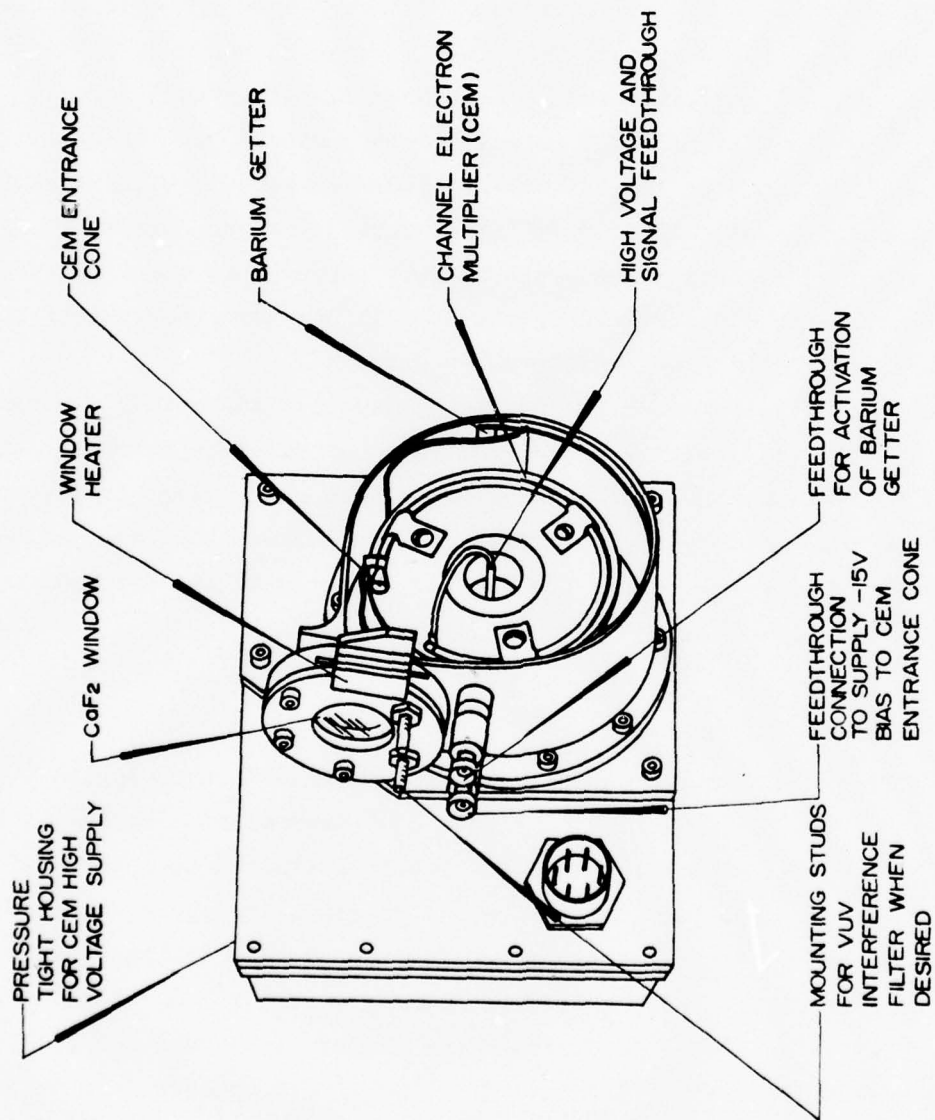


Figure 20. View of CEM detector for 0 measurement with lid cut away.

contamination from high vapor pressure materials and especially fingerprints. All internal metal components are cleaned prior to assembly by blasting with glass beads. The vacuum seals are by Viton O-rings which are totally free of grease to allow the entire assembly to be outgassed at moderate ($\approx 350^{\circ}\text{F}$) temperatures during pumping.

The UV entrance window is a commercial bakeable CaF_2 window in a Varian conflat flange which has been slightly modified to minimize the window to detector separation distance. Provision is made in the window mounting for the addition of heating and/or auxiliary filters which are required for measurements under daylight conditions.

After assembly the detector is pumped for approximately 20 hours, utilizing a liquid nitrogen trapped helium mass spectrometer leak detector. This provides not only a clean pumping system, but also the ability to determine the presence of leaks. The majority of the pumping is done while the detector is held at 350°F in an oven. After the pumping and outgassing process is completed, a barium (≈ 5 mg released barium) getter is outgassed by passing current through the getter of a magnitude just below where barium would be released. After the evolved gas is pumped, the getter current is increased to release the metallic barium. The getters are shielded to prevent barium vapor from reaching the CEM and altering its performance. Particular attention is given to preventing barium vapor from reaching the entrance cone where it could materially alter the CEM spectral response. As soon as the getter has been flashed, the detector tubulation is pinched off from the pump.

During the pumping operation, considerable difficulty was experienced with leaks. In most all cases the leaks were not in the welds or seals where they might have been expected, but were directly through the machined stainless steel housing. The leaks would most often not be discovered until the detector had been baked, and in a number of cases only during bake. These leaks were evidently due to a defect running along the axis of the stainless steel bar from which the housings were machined. In some cases the leaks could only be sealed from the outside using a vacuum epoxy (Varian Torr Seal). Although this is a very undesirable procedure from the standpoint of producing a clean vacuum, it was successful and resulted in detectors that remained operational for several months before they were finally flown.

Additional rejection of both Lyman- α at 121.6 nm and mid-ultraviolet may be obtained by including an interference filter in front of the detector. Although vacuum UV interference filters are a relatively new technology, some improvement may be realized at the expense of a loss in sensitivity. The filter shown in Figure 21 was built on a CaF_2 substrate 2 mm thick by Acton Research. It has a 19.5% peak transmission at 130.4 nm and a bandwidth of 16.5 nm F.W.H.M. at 78 F. This bandwidth can be expected to reduce as the filter is heated due to a shift in the short wavelength cut-off of the CaF_2 .

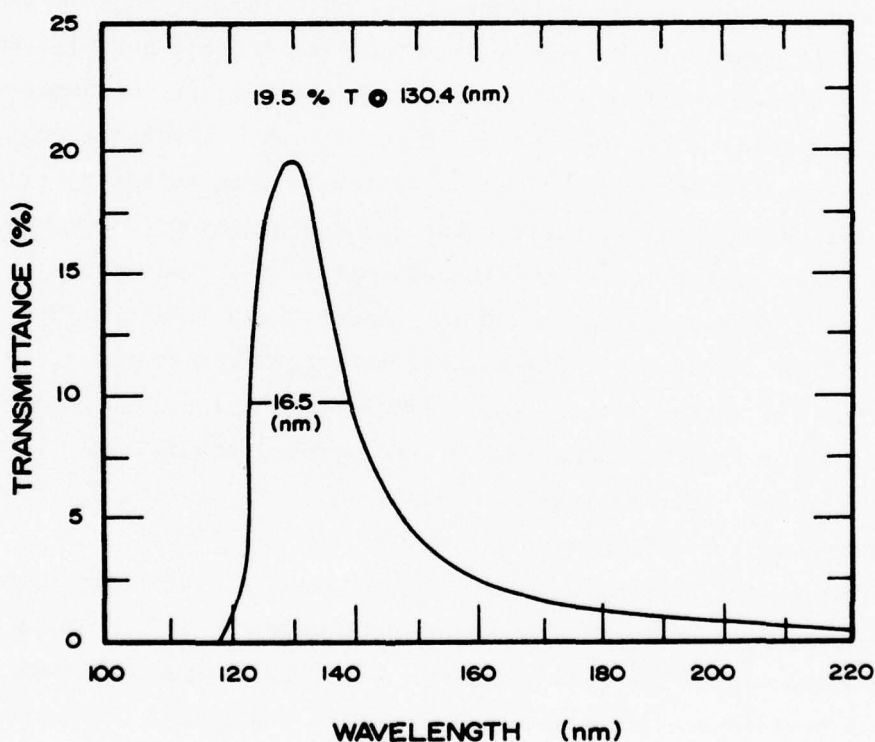


Figure 21. Spectral transmission of a VUV interference filter built on a CaF_2 substrate at 78 F. As temperature is increased, the shorter wavelength cutoff will increase further decreasing the bandwidth and improving the rejection of 121.6 nm H Lyman- α .

PAYLOAD DESIGN

Some of the guiding requirements dictating the payload design for the initial test flights of the atomic oxygen system were the necessity of using a relatively small (6" diameter) Astrobe D motor, a White Sands Missile Range launch site, achieving an altitude of at least 120 km, and an attempt at both day and night measurements.

Inasmuch as the single stage solid fuel Astrobe D is not capable of altitudes much above 100 km with a payload weight of 30 lbs., considerable attention was given to making the payload as light as possible. The Astrobe D also has high velocities at relatively low altitudes, and aerodynamic loading and skin heating are significant design considerations.

The general configuration of the instruments was a horizontally mounted light source with the detector mounted below, viewing a segment of the light beam. This required a single door to be opened in the skin rather than ejecting a portion of the nose cone for a forward looking configuration. The payload configuration is shown in Figure 22. The atomic oxygen resonance lamp and detector are side-looking with an intersection point for the conical fields of view being six inches from the resonance lamp exit window. Immediately above the resonance lamp and looking through the same ejectable door is either an IR horizon sensor for night flights or a solar aspect sensor for daytime flights to help in determining the payload attitude. A magnetic aspect sensor mounted across the longitudinal axis of the rocket also aids in determining the vehicle dynamics.

All of the electronic circuitry for payload control, monitoring, and signal conditioning are mounted on open cards above the magnetic aspect sensor. The open card approach was chosen in favor of putting the electronics in an enclosed box mounted to a deck because of space and weight considerations. Power for all of the electronics including telemetry and the resonance lamp is supplied from a set of 1A-Hr NiCd batteries. Above the payload batteries is the electronics pertaining to the resonance lamp with the exception of the RF power oscillator which is located in the same housing as the resonance lamp. A separate NiCd battery to operate the guillotine used to open the door is located

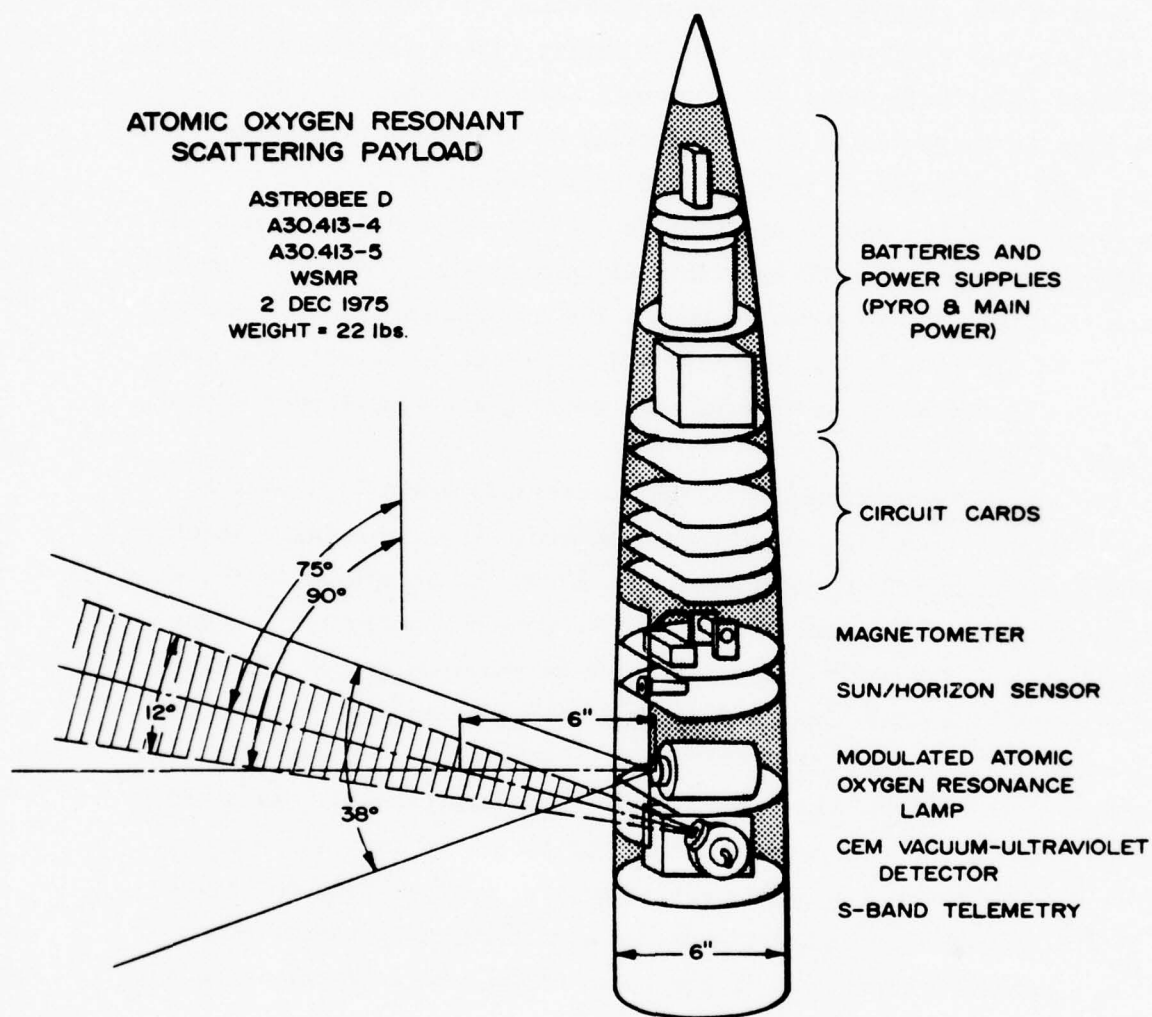


Figure 22. Astrobee D payload carrying a resonant scattering atomic oxygen measurement.

along with an acceleration activated switch in the far forward portion of the payload.

At the far back end of the payload in a section that is readily separable is the telemetry transmitter and ranging receiver. The transmitter operates at 2269.5 MHz in the S-band at 2 watts output. Five fm/fm IRIG subcarriers were used and the antenna was a circularly polarized flush mounted strip line. Details of the telemetry assignments are included in the appendix.

Atomic Oxygen Instrumentation Electronics

In order to separate the signal contribution from steady background sources, it is necessary to use a 50% duty cycle modulated light source. The counts measured with the lamp off may then be subtracted from those with the lamp on to find the true amount of scattered light. Since a subtraction will be necessary and also because of the wide dynamic range of the measurement, a digital data handling approach is most appropriate. The hybrid PCM, PAM format shown in Figure 23 was selected for its versatility and ease of implementation. The format consists of frames of 24 bit digital binary outputs at a rate of 50 frames/sec (1200 bps). Not all of the bits carry detector count rate information in that five bits per frame are used for a PCM/PAM synchronization. These sync bits are a zero (lower band on an fm/fm channel) followed by three ones (upper band edge on an fm/fm channel) followed by another zero. All other binary data bits are only about 70% of upper band edge for a 1 and lower band edge for a 0. The characteristic synchronizing bit pattern will allow PCM decommutation and the amplitude differences between synchronizing and data bits will allow PAM decommutation in the same way as a standard PAM multiplexer may be handled.

The binary data which is in reality a count of the detector output during one-half of the lamp modulation cycle is presented most significant bit first with the first bit (which would have been 2^{18}) always high. All other bits from 2^{17} to 2^0 are valid data bits.

Since the lamp will be square wave modulated with a 50% duty cycle at a 50 Hz rate, the lamp will be on for 10 ms and off for 10 ms. This means that the binary number in one data frame when converted to decimal and multiplied by 100 will be the detector count rate in counts/second.

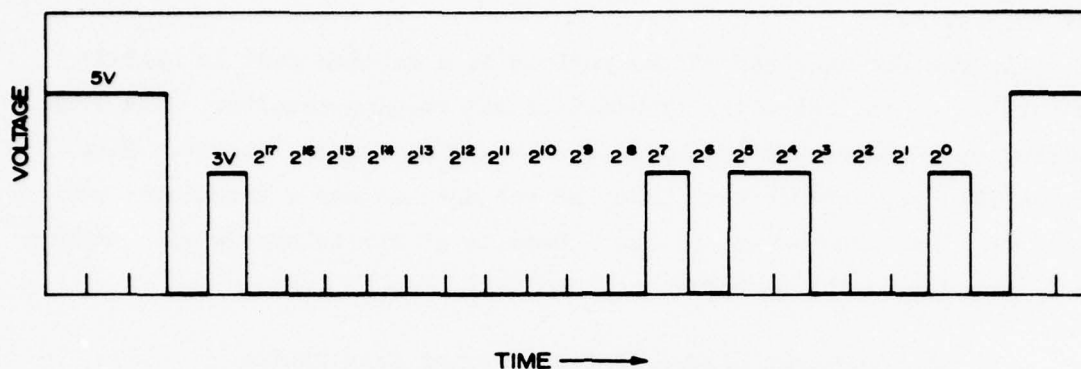


Figure 23. Hybrid PCM/PAM digital format used. The count rate is straight binary coded and represents counts/ 10^{-2} sec. Two such simultaneous formats are produced providing a separate channel for both lamp on and lamp off conditions. This format may be read by both PCM equipment as well as by PAM decommutation devices.

The binary output shown in Figure 23 represents a count rate of 17,700 counts/second.

Rather than accomplish the subtraction of background count rate from lamp on count rate, the count rates will be sent in parallel (clocked out simultaneously) through two separate fm/fm telemetry channels.

The circuitry required for the above implementation is shown in Figure 24. The signal from the CEM is a quantity of charge of approximately 10^8 electrons or 1.6×10^{-11} coulombs. This charge is fed into an operational amplifier integrator having a feedback capacitor of about 5 pf and is in parallel with a 200 meg resistor. The resulting output is a voltage step of approximately 3.2 volts decaying with a 3.2 ms time constant. This waveform is differentiated and integrated through 5 μ sec time constants which produces a standard pulse shape without serious overlap up to 10^5 counts/sec while eliminating virtually all low frequency drifts and noise. If the pulses exceed a predetermined threshold, they are amplified, squared, and sent to a set of steering gates. When the lamp is on, the gates direct the count signal to a 18 bit binary counter which accumulates all of the counts during the 10 ms on period. If the

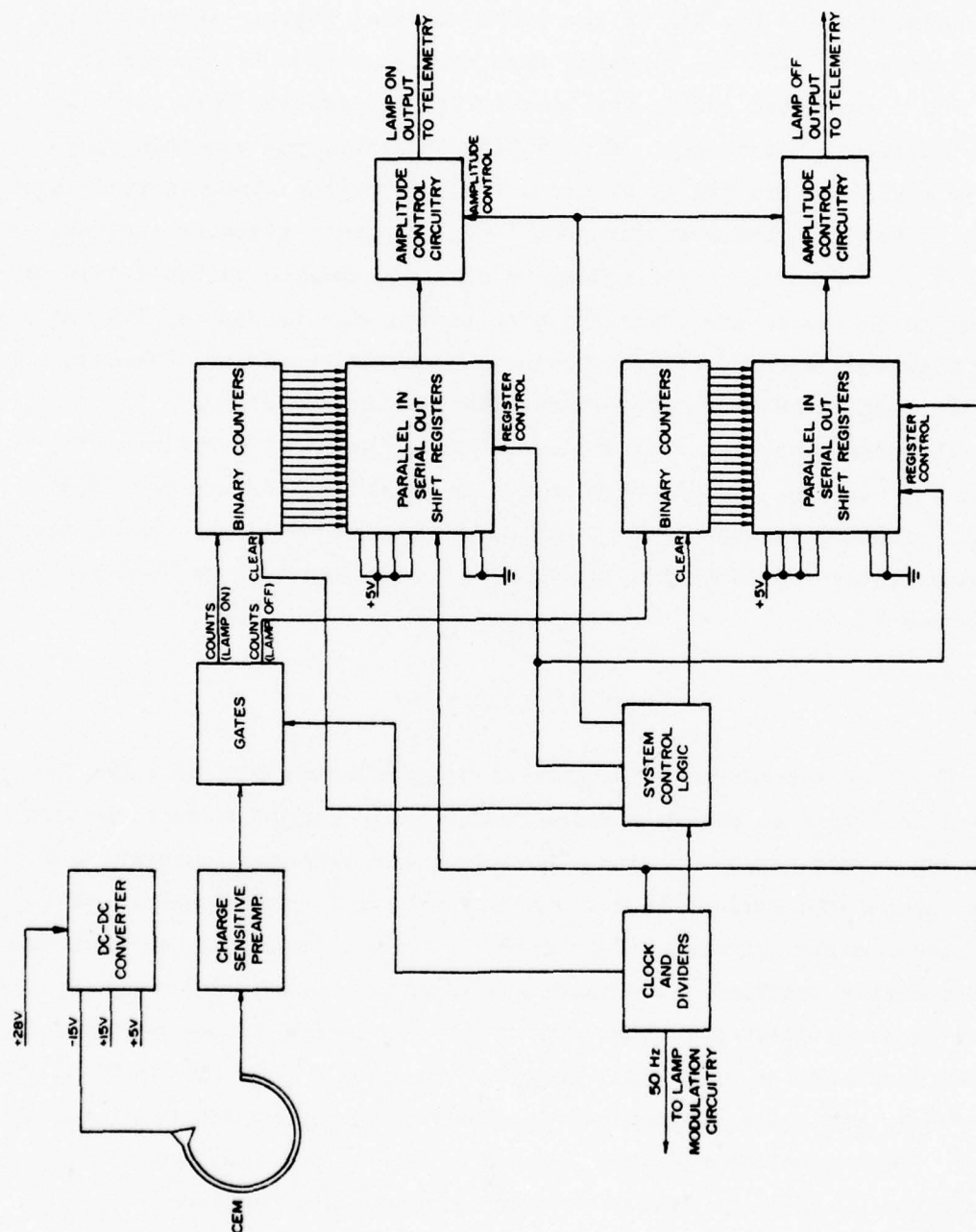


Figure 24. Block diagram of the flight atomic oxygen measurement system.

lamp is off, the counts are directed to a similar accumulating counter.

The logic gates steering the counts to the proper counters are controlled by a master system clock. This clock provides the drive for the lamp modulator and for all of the system control logic. Additionally, it provides the 1200 bps clocking for the data output to telemetry.

The accumulated counts are transferred in parallel into a 24 bit shift register. Since only 18 data bits transfer, the remaining positions in the registers are filled by wired inputs with the appropriate ones and zeros to form the frame synchronization. The shift register contents are shifted out serially to the telemetry system through a variable gain amplifier which causes the frame synchronization bits to pass at full amplitude required for band edge to band edge modulation of the telemetry sub-carrier. All other bits are passed with reduced amplitude.

The remaining electronics are associated with monitor circuitry, control circuitry, and pyrotechnic timing circuitry and are not unique to the atomic oxygen payloads. Consequently, they will not be described in this report. Calibration information on all monitors is included in the appendix.

SYSTEM CALIBRATION

There is a considerable number of factors which must be taken into account in order to obtain a valid relationship between a detector count rate and atomic oxygen density. Obviously the simplest calibration would be to operate the payload in a known atomic oxygen environment to obtain the needed calibrations. Unfortunately, a known atomic oxygen environment is not easily obtained. The extremely reactive nature of O necessitates a low pressure flowing system. The large scattering volume represented by the intersection of a light emission cone and a detector field of view cone would require a large flowing volume with uniform atomic oxygen density. These requirements when coupled with cost and time considerations forced the decision to seek secondary calibration techniques.

The calibration method utilized involved determining all of the physical parameters involved with the scattering system and then from the fundamental physical principles of resonant scattering derive a "transfer function" between count rate and oxygen density. The scat-

tering process itself as previously described requires a knowledge of such items as listed in Table 2.

Table 2
EVALUATION OF RESONANT SCATTERING PARAMETERS

Resonant Scattering Parameter	How Evaluated	Accuracy
Oscillator strength (f-number)	Published measurements	Very good $\approx \pm 2\%$
Scatterer temperature	Atmospheric models	Fair
Lamp emission temperature	Line width measurements on similar lamps and modulation in the data due to Doppler effect from the rocket velocity	Fair to poor
Emission line shape (pure Doppler with negligible self-absorption)	Emission line height ratios and knowledge of lamp operating conditions	Fair

Although this table does not reflect all of the assumptions required in describing the resonance interaction, it does include some of the more important parameters with associated assumptions and an indication of how reliably they were obtained.

In addition to the above parameters relating to the resonant-scattering interaction, other parameters must be evaluated which are of a geometrical nature resulting from the physical configuration of components within the payload and the responses of the components. These other parameters are summarized in Table 3.

As indicated in Table 3, one of the important parameters needed for data evaluation is an accurate measure of lamp intensity. This was accomplished in a large vacuum chamber where the resonance lamp could be placed at a distance of approximately one meter from a calibrated photodiode. By knowing the diode quantum efficiency, geometry, and diode current, the lamp intensity could be calculated. Several types of diodes were used as cross calibrations. One was an aluminum oxide diode calibrated by NBS at a number of wavelengths including H Lyman- α at 121.6 nm which was the longest wavelength measured. It was therefore necessary to extrapolate

Table 3
EVALUATION OF GEOMETRICAL AND COMPONENT RESPONSE PARAMETERS

Parameter	How Evaluated	Accuracy
Lamp intensity	Calibrated diode and geometry	Fair ($\pm 30\%$)
Detector Quantum Efficiency	0 lamp, geometry, and detector sensitive area	Fair to poor ($\pm 50\%$)
Lamp intensity variation with angle off optical axis	Measurement with standard diode	Good
Scattering geometry	Measurement of lamp emitting dimensions, optical baffle dimensions and positions, angles between light source and detector axes	Good
Second order geometry effects (light source being partially obscured by its optical baffle near the edges of the light cone, etc.)	Calculated from measured geometry	Good
Attenuation of lamp	From measured [0] effective cross section and geometry	Fair

the response about 11.9 nm to the oxygen wavelengths. Another diode produced by EMR was used before, and finally a pair of LiF window NO-filled ionization chambers were used since their QE at 121.6 nm was reasonably well-known and the response of NO between 121.6 and 130.6 nm has been measured.

Unfortunately, none of the diodes were well-calibrated for our purpose and their agreement was not particularly good. All of the detectors except the NO cell were not only sensitive to the oxygen triplet, but were also sensitive to the emission of significant intensity at 135.2 nm. Since the vacuum system had to be opened each time the measurement set-up was changed (which required nearly a half day) and the lamp could not be left running, part of the variations were certainly due to variations in the lamp itself. For the above reasons the accuracy in the absolute lamp intensity measurements was not better than $\pm 30\%$.

The emission spectrum of a typical lamp is shown in Figure 9. As indicated, the line height ratios are 4.3, 2.7, 1, and the measured on

axis intensity was 6.2×10^{12} photons (sec steradian).

The variation of lamp intensity with angle from the optical axis was measured with the same setup used for the intensity measurements except that the lamp could be rotated to any desired off-axis direction. The results of these measurements are shown in Figure 10. It should be noted that only four points were actually measured due to the vacuum system cycle time and that the distribution was considered to be cylindrically symmetrical about the optical axis.

The detector quantum efficiency was measured using the previously measured oxygen resonance lamp as a light source. In this case the detector was located at a distance of approximately 3 meters from the lamp. Inasmuch as the photon flux was larger than was desirable, a precision etched metal screen of approximately 100 mesh and very well known transmission (9.13% transmission) was used directly in front of the detector window. After evaluating the geometry, it appeared that the detector quantum efficiency was significantly (a factor of between 4 and 8) below that which was anticipated from the published quantum efficiency. Furthermore, the measured quantum efficiency was much more voltage sensitive than was anticipated for a photon counting system.

Several different effects could account for the low measured quantum efficiency. These include attenuation in the vacuum chamber due to N_2 and O_2 and also perhaps to contaminants such as diffusion pump oil (the chamber was refrigeration trapped). The more likely source of low quantum efficiency was discovered after consulting with Galileo engineers and was supported by the larger than expected change in count rate with changing CEM operating voltage.

As shown in the cross section of the entrance cone to the CEM in Figure 25, the potential gradient is determined by the resistance of the semiconductive coating on the surface of the cone. Near the mouth of the cone there is a considerable lower potential gradient than further down in the cone. The lower gradient reduces the probability that secondary electrons will be produced when the initial photoelectron strikes the wall. Since the field gradient in the cone is directly proportional to the CEM operating voltage, the probability of producing secondary electrons from the initial photoelectron also increases. The response of the CEM in terms of an overall quantum efficiency can be thought of

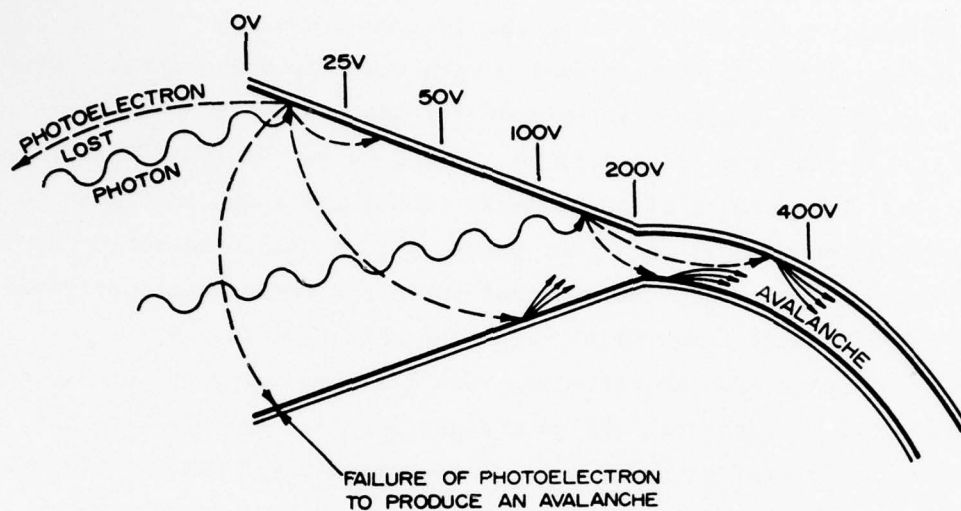


Figure 25. Since the potential gradient along the CEM entrance cone is nonlinear with distance and the lower gradient is nearest to the cone mouth, the probability of producing a photoelectron which will fail to initiate an avalanche is considerably higher near the mouth.

as the product of the photocathode quantum efficiency and the secondary emission efficiency of the photoelectrons. This secondary emission efficiency for the photoelectrons is a function of the CEM entrance funnel shape and also the position on the funnel that the photoelectron is generated. This effect is analogous to the first dynode collection efficiency in a conventional photomultiplier. Although the reduced overall quantum efficiency due to reduced secondary emission efficiency was known to the manufacturer, we were unaware of the problem and its relatively simple solution used in photon counting applications: addition of a straight 0.15-inch extension to the front of the CEM entrance cone to produce a field configuration more favorable to increased secondary emission efficiency.

Although neither the lamp intensity nor the detector quantum efficiency or actual detector area could be measured with very good accuracy, the ability to accurately measure atomic oxygen is not correspondingly impaired. This is true since the detector count rate in an atomic oxygen

measurement is proportional to the product of the lamp intensity and the detector quantum efficiency, and if this product is accurately known, then the accuracy of the individual factors is irrelevant. When the detector quantum efficiency was measured using the resonance lamp and the actual detector in simple geometry, in effect, this important product of intensity, efficiency, and detector area was being measured with very good accuracy (better than $\pm 1\%$).

The remaining considerations to be evaluated are those relating to geometry, i.e., the lamp emissions as functions of angles, and the detector field of view again in relation to the lamp emissions. The approach taken to all of these scattering geometry considerations was to include all geometrical relations for the lamp and detector together with an effective scattering cross section and an assumed 0 density and incorporate them into a computer model to calculate the anticipated count rate. Attenuation of the primary light beam and the scattered resonance radiation were included as a first order approximation to what could become a complex radiative transport problem. This simplification is reasonably well justified in that even at maximum anticipated 0 density the factor $k_0 l$ is small. Similarly, line broadening was ignored in favor of considering the lines to have a Doppler distribution.

The geometry of the intersection of the light source and detector fields is shown in Figure 26. Since the aperture determining the emission cone from the lamp is near the lamp and the lamp exit window is large, the beam is not sharply defined. The center section of the beam (9.9° full angle) is all that is not occluded by the lamp aperture. In the region behind 9.9° out to 62.2° , the lamp emissions are partially occluded by the aperture. A similar situation exists with the detector except that the detector area is much smaller with a much larger distance to the aperture. In the case of the detector, the unoccluded angle is 12° and the angle to the outer edge of the partially occluded region is 14.8° .

Inasmuch as the computer program performs a numerical integration of the photons from elemental scattering volumes that reach the detector, it is necessary to accurately define the occlusion processes. This is especially important in the primary beam since it has a very large portion of the beam partially occluded.

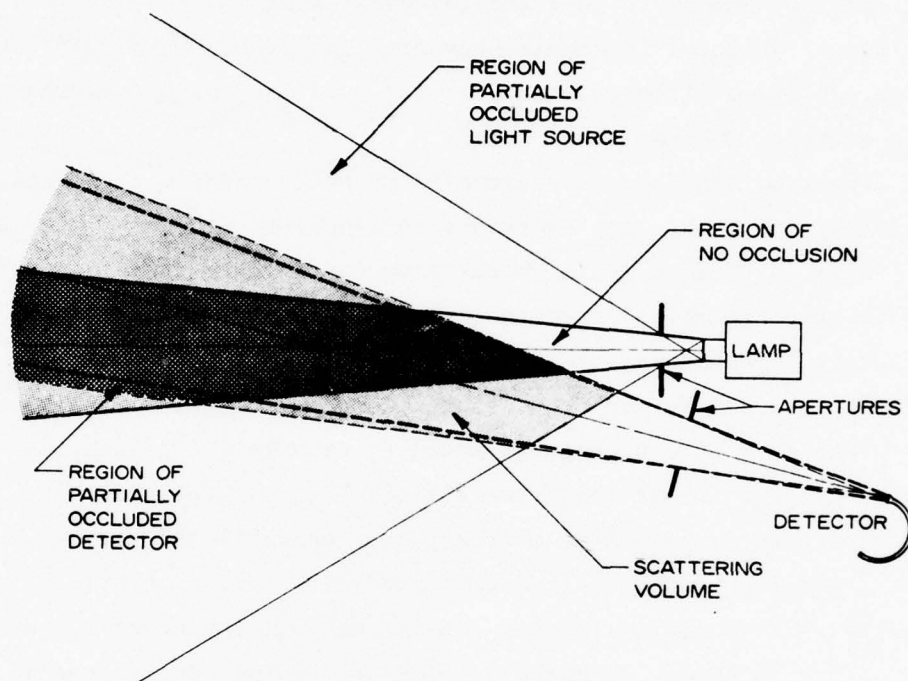


Figure 26. Intersection of two conical fields, one from the light source and the second being the detection field of view. The intersection of these fields is the scattering volume for which an evaluation must be made for all regions - those with no occlusion and those with partial occlusion.

The variation in lamp intensity with angle from the optical axis due to occlusion reduces to a geometrical problem consisting of two apertures having radii R_A and R_D as shown in Figure 27. Since there are no non-linear effects involved and the geometry is reciprocal, it follows that the throughput of the pair of apertures makes no difference which direction the light may be traveling. The effects of geometry are most readily visualized by considering a source of parallel light rays at an angle θ from an axis normal to the two apertures and passing through their center. The amount of the projected aperture of radius R_A overlapping the aperture R_D defines the fractional throughput. The variation in fractional throughput as a function of θ defines the manner in which partial occlusion due to the aperture reduces the off-axis lamp output.

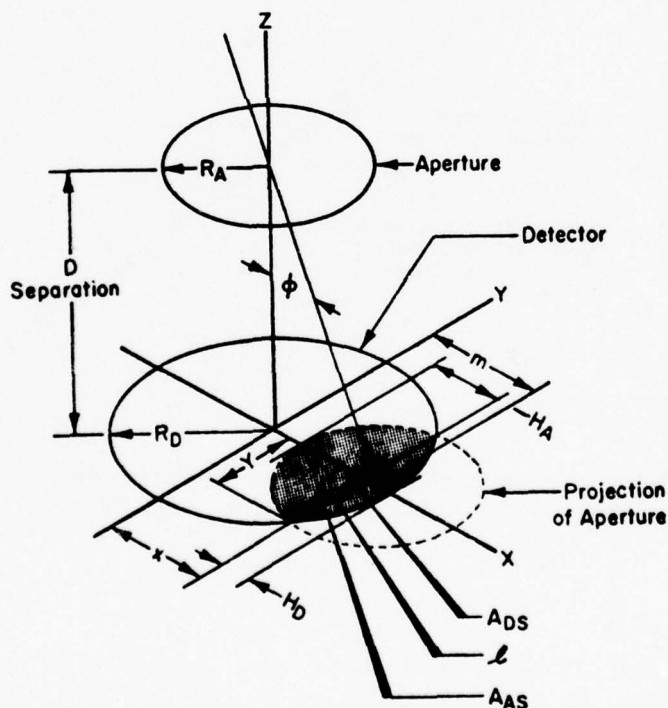


Figure 27. The regions of partial occlusion may be treated by an analysis of the throughput from two apertures as a point light source at infinity travels through an angle θ varying from 0 to 90°.

Figure 28 shows the calculated lamp intensity as a function of angle θ compared with an assumed linear decrease in intensity with between θ_{\min} (no occlusion) to θ_{\max} (total occlusion). Obviously good accuracy in defining the atomic oxygen scattering processes requires the use of the calculated lamp intensity. Since the lamp output exclusive of any occlusion due to baffles is directional due to the shape of the emitting volume as shown in Figure 9, this variation in intensity must be combined with the occlusion to determine the total effect.

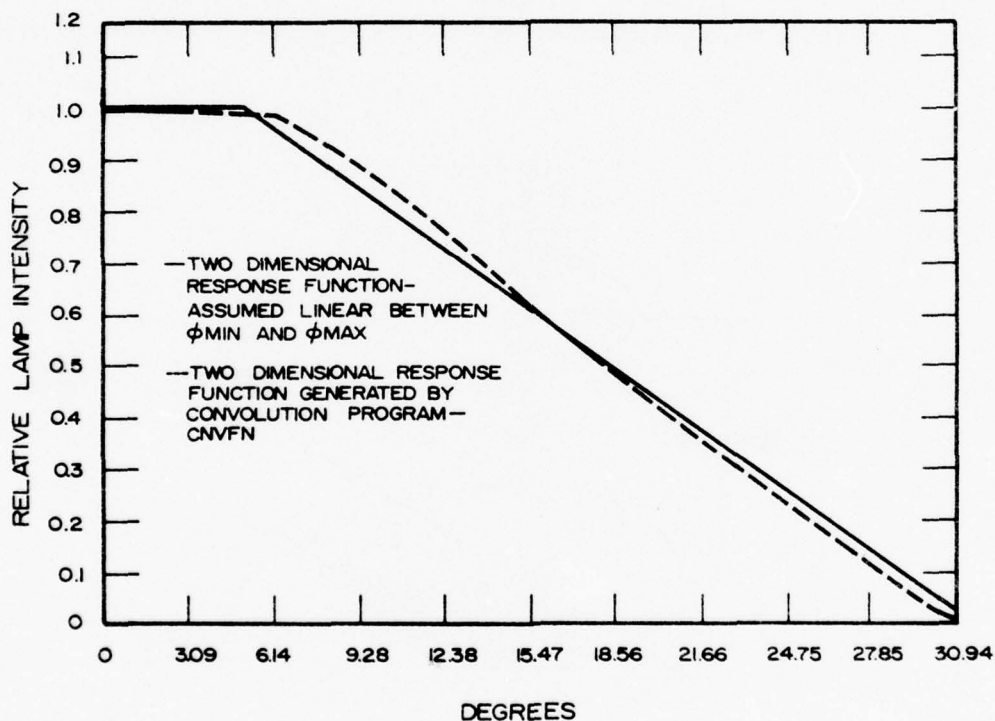


Figure 28. Calculated variation of lamp intensity as a function of angle due to partial occlusion by the baffle in front of the lamp. This assumes an isotropic light source and does not include the effects of lamp directionality shown in Figure 10. Also shown is a linear approximation to the occlusion effect.

Once the light source and detector field of view geometry have been characterized by the above described techniques, the process of numerical integration over the scattering volume can be accomplished. Figure 29 shows the scattering geometry in detail including the coordinate systems used in the integration. Integration is done by considering a small integrating element ΔV (DV in program). The complete computer program is included in Appendix A. As shown in Figure 29, the origin is located at the nearest point of intersection of the two cones. As long as the element is located inside this intersection, the integration is accumulated. The origin was chosen to accomplish this by stepping in the negative "y" direction until outside the intersection, stepping in the "z" direction when "y" stepping leaves the intersection and after setting "y" to zero, and the stepping in the "x" direction when the other two directions exceed the intersection. To accomplish the integration efficiently, the length of the sides are doubled each time the distance from the origin is doubled.

In order to determine whether the ΔV is inside the intersection of the two cones, the subroutine DCONE and SCONE are used. These subroutines convert from a rectangular coordinate system in E^2 to polar systems centered at the detector and lamp respectively.

After an integrating element has been established that satisfied the requirements of DCONE and SCONE, i.e., it is considered to be a valid scattering volume, the intensity of resonance emissions at the volume are calculated. The total number of scattered photons is calculated from an effective cross section and an assumed 0 density. The probability of one of these photons entering the detector is calculated and then, after correcting the intensity for absorption along the total optical path, the ratio between observed counts and the 0 density is established.

Inasmuch as the scattering volume extends to an infinite distance from the measuring payload, the relative contribution to the total return signal were investigated as functions of both distance from the payload and the density as shown in Figure 30. Nearer to the rocket payload than 14 cm there will be no scattering since the scattering volume goes to zero. The integral volumetric contribution per atom increases very rapidly with distance beyond 14.5 cm and gradually levels out beyond 100 cm. As ex-

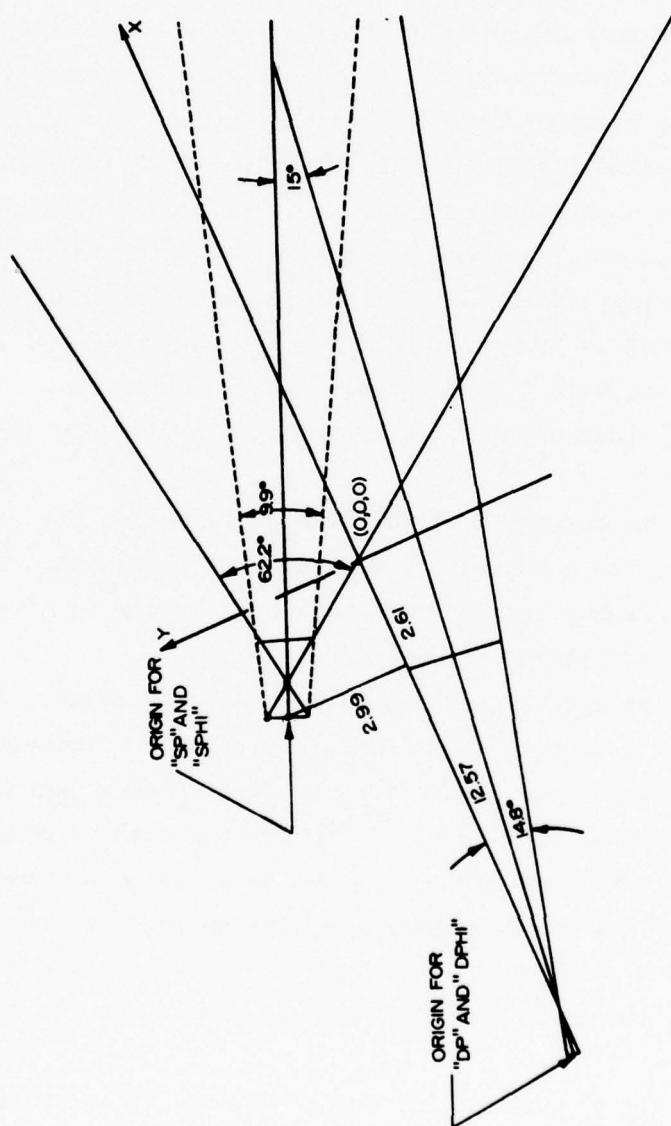


Figure 29. Detail of the coordinate system used for the computer evaluation of the atomic oxygen scattering geometry.

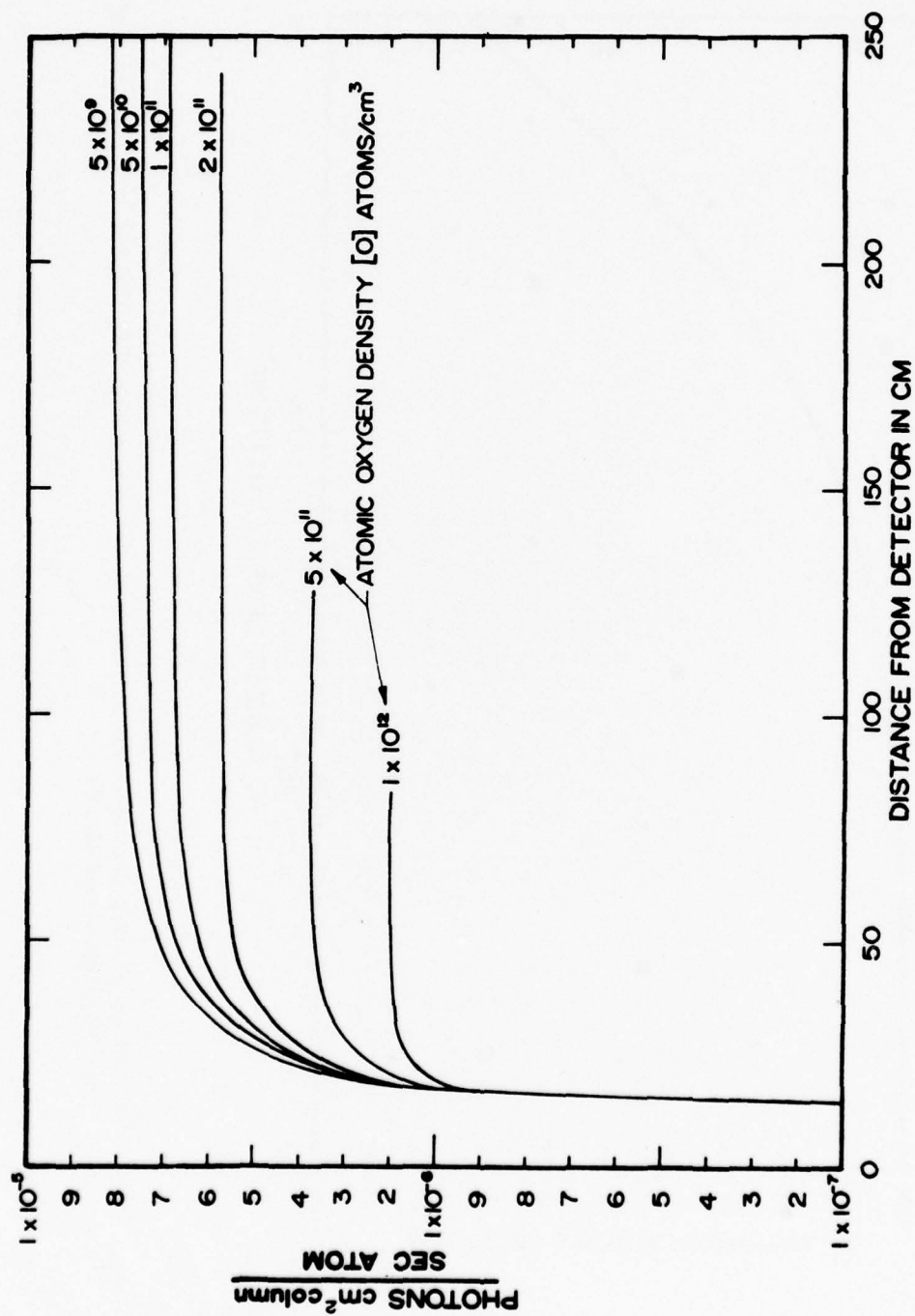


Figure 30. Integral of contribution to count rate per O atom as a function of distance from the detector. In all cases the contributions from scatters beyond 1 meter is small and the significant effects of absorption are most evident at densities of 10^{11} O atoms/cm³ and higher.

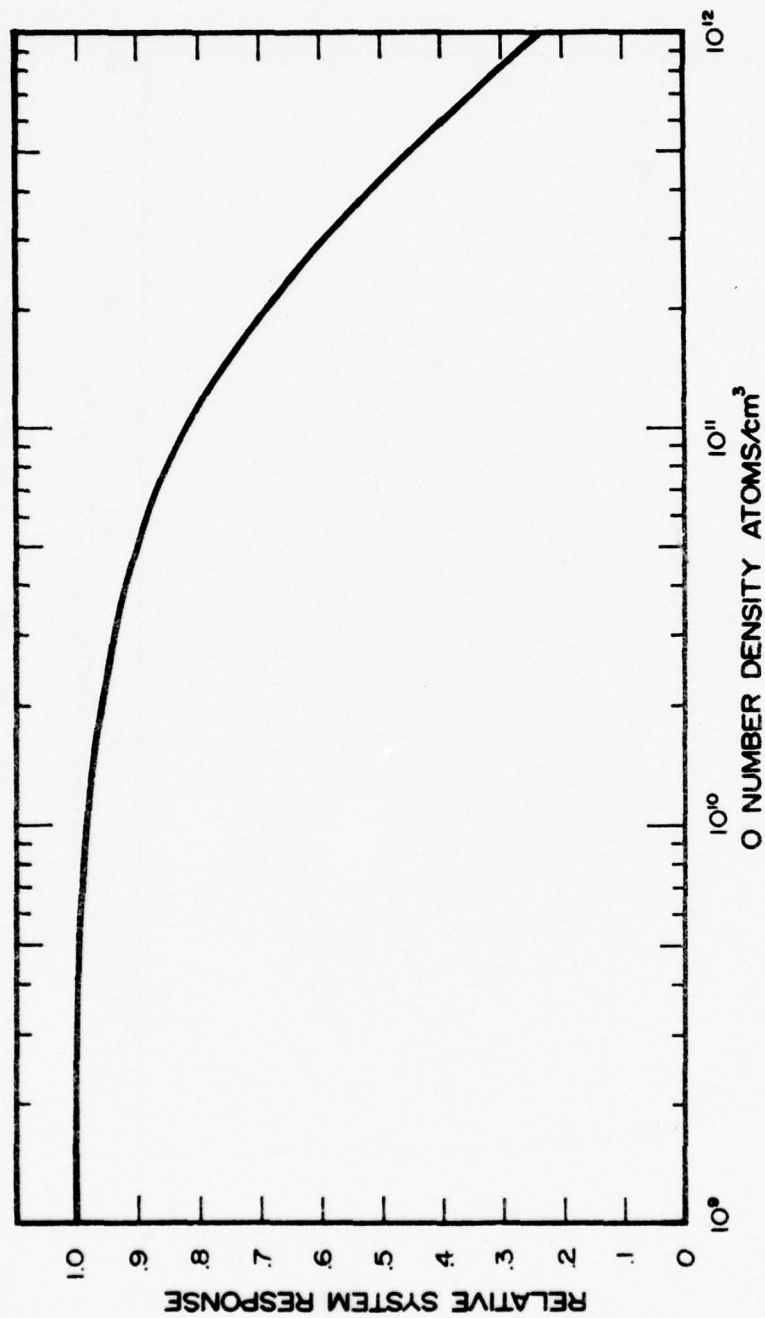


Figure 31. Relative system response as a function of O density showing the effects of absorption at higher densities.

pected, the contribution per atom will be largest at low densities since there is little absorption. It should also be noted that the curves representing high densities, i.e. 1×10^{12} and 5×10^{11} atoms/cm³, are virtually flat beyond about 50 cm indicating that absorption eliminates all contribution from scatters beyond 50 cm. At low densities, i.e. 5×10^9 atoms/cm³, the distant contribution out to a few meters is still significant.

The effect of attenuation, again using the simple absorption model and neglecting multiple scattering and spectral hardening effects, is shown in Figure 31. As may be noted, the corrections required for densities below 10^{10} atoms/cm³ are minimal. For densities of 10^{11} atoms/cm³ the corrections become quite significant and for densities of 10^{12} atoms/cm³ the corrections are large and all of the simplifying assumptions become questionable and should be more accurately evaluated.

FLIGHT RESULTS

Two Astrobee D payloads for measurement of atomic oxygen (A30.413-3 and A30.413-5) were developed for flight before and after sunset. The system in rocket A30.413-5 which was flown during daytime conditions just after local sunset 1735:23.8 MST on 2 December 1975 (before sunset at altitude) was equipped with an interference filter and heated window in front of the detector to provide additional rejection against mid-UV solar emissions.

On this flight it appears that the door covering the instrumentation came off at low altitude. Since the preamplifier for the detector was located on a longeron immediately next to the door, it was subjected to excessive heating. Later in the flight as it cooled, it began to again function, although its characteristics did not stabilize sufficiently to obtain data of sufficient quality to be of much use in accurately defining the character of the atomic oxygen profile. The flight, however, was a useful demonstration of the practicality of using this system under daylight conditions.

The second payload was launched slightly less than 1½ hours later at ~ 19:00 local time. This payload performed normally in all respects and provided excellent data. A ground-based 557.7 nm photometer pointed

toward zenith provided a supporting measurement of integrated atomic oxygen as a useful cross correlation.

The detector count rate after subtraction of the background count is shown in Figures 32 and 33 for the upleg and downleg of the rocket trajectory, respectively. The data shown represents a 3 second running average taken every second. As may be noted, there is considerable structure evident on both up and down legs, although the structure is not identical in both directions. The most notable structure exists at an altitude of approximately 94 km with evidence for additional structure at lower altitudes, in particular at about 84 km. The statistical significance of variations will be discussed later.

As previously indicated, the conversion between detected count rates and O density deviates from a simple linear conversion by dependence upon absorber temperature and O density itself (absorption). The temperature model used comes from the 45°N January profiles with an exospheric temperature of 900°K. When these corrections have been applied to height profiles of atomic oxygen density, up and down legs become as shown in Figures 34 and 35, respectively. Figure 34 also carries a set of error bars labeled relative error and absolute error. The relative error bars result from statistical variations, incorrect knowledge of the atmospheric temperature profiles, and inadequate absorption models that would alter the relative shape of the measured profiles. The wider absolute error bars reflect the effects from all sources leading to uncertainties in the determination of absolute atomic oxygen density.

By reducing the data with different smoothing techniques, some of the spatial structure smoothed over by the averaging shown in previous figures becomes more apparent at the cost of less statistical accuracy. A segment of the up leg data between 78 and 105 km is shown in Figure 36 and for down leg data in Figure 37. Substantial amounts of structure are seen in the upleg data where comparatively little with the exception of around 94 km is apparent in the down leg. These data were processed using a 1 second running average taken every .1 second.

Plotting these data on an expanded altitude scale for the major O density dip at 94 km on the up leg in Figure 38, the statistical significance of the departure from a smooth profile is apparent. Figure 38 shows both the plotted points and a smooth curve representing the anticipated

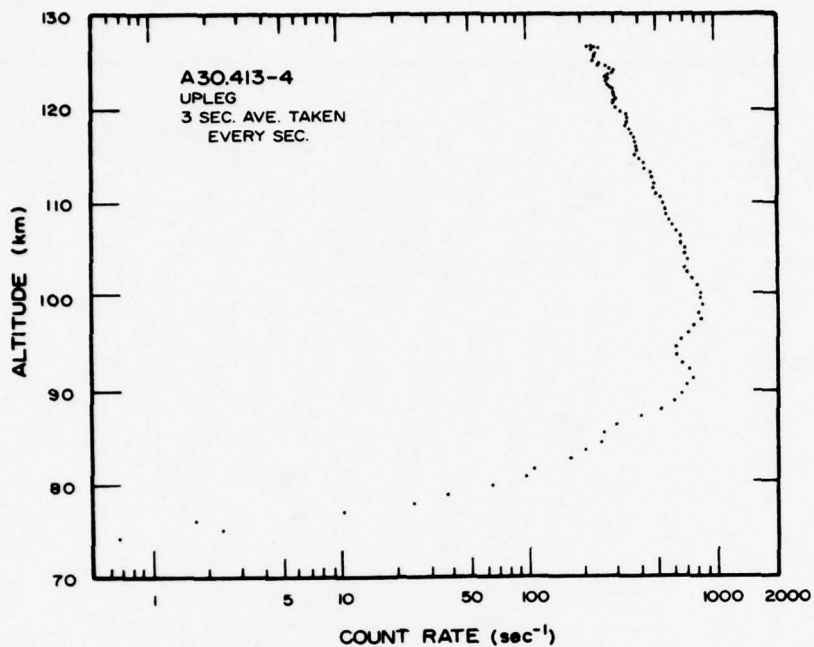


Figure 32. Upleg atomic oxygen raw data with background subtracted for Astrobe D A30.413-4 launched at WSMR on 2 December 1975 at 19:00 local time. Data shown with a 3 sec running average shown every 1 second.

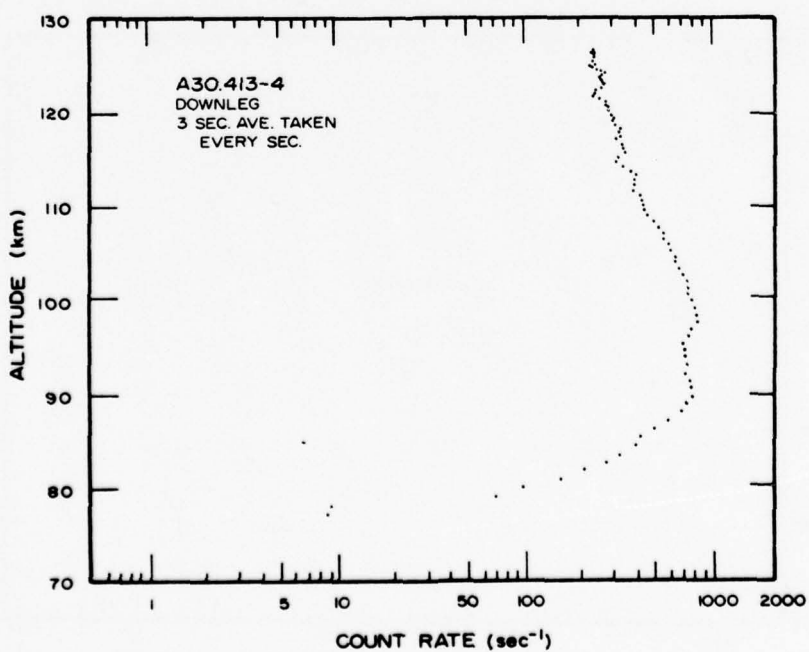


Figure 33. Downleg atomic oxygen.

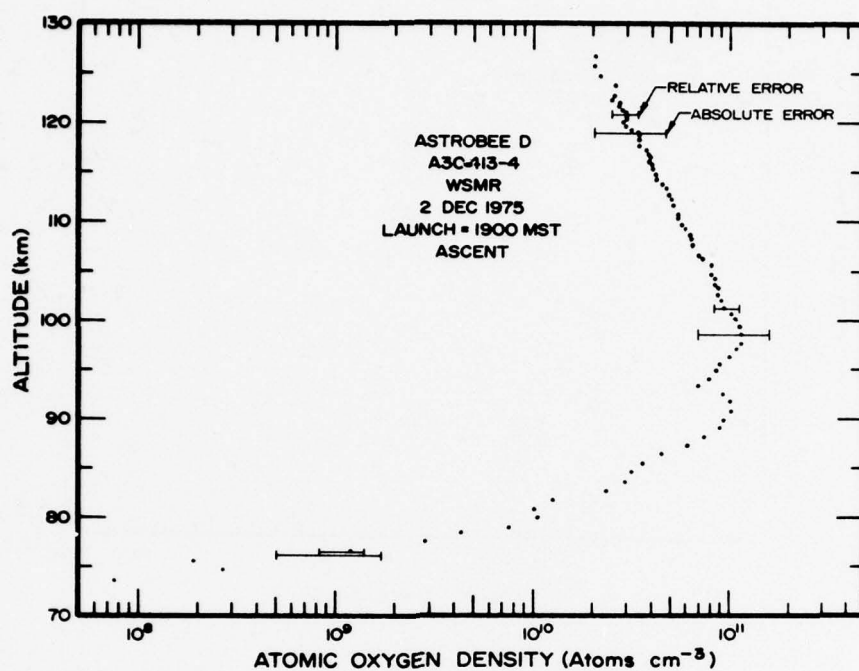


Figure 34. Atomic oxygen data in terms of O density showing an estimation of relative and absolute errors. Three second average taken every second.

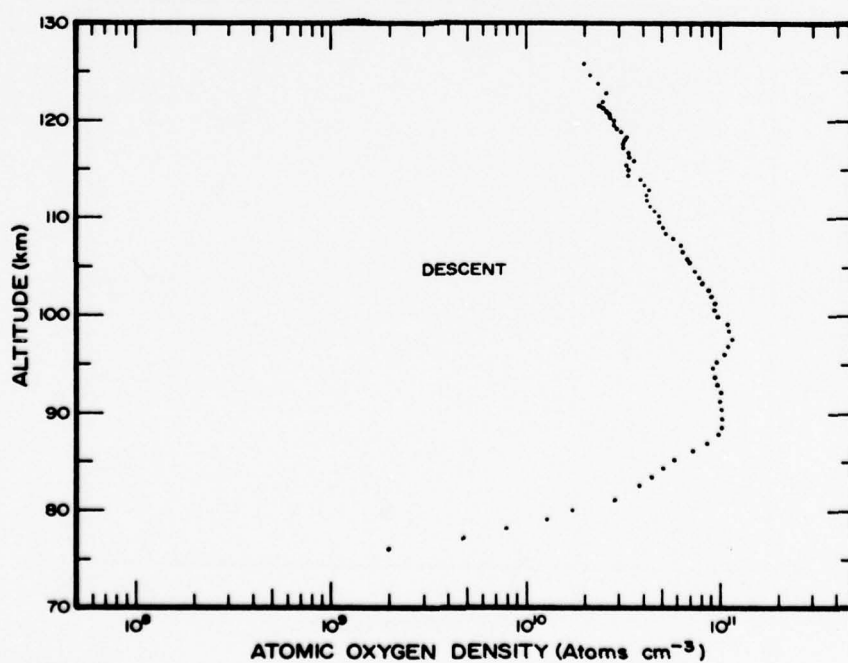


Figure 35. Atomic oxygen descent data.

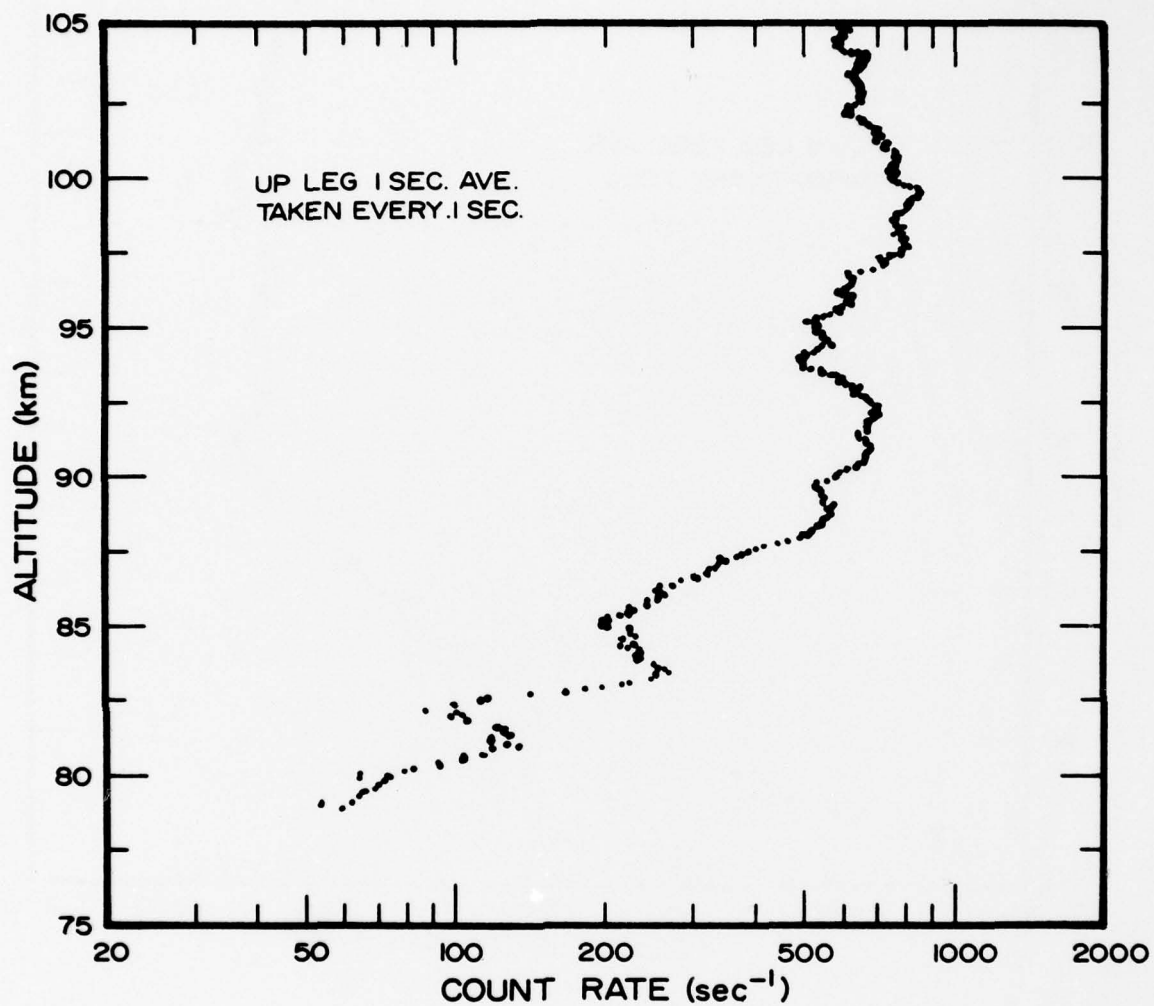


Figure 36. High resolution data showing considerable structure. Data reduced with 1 second running average taken every .1 sec up leg data.

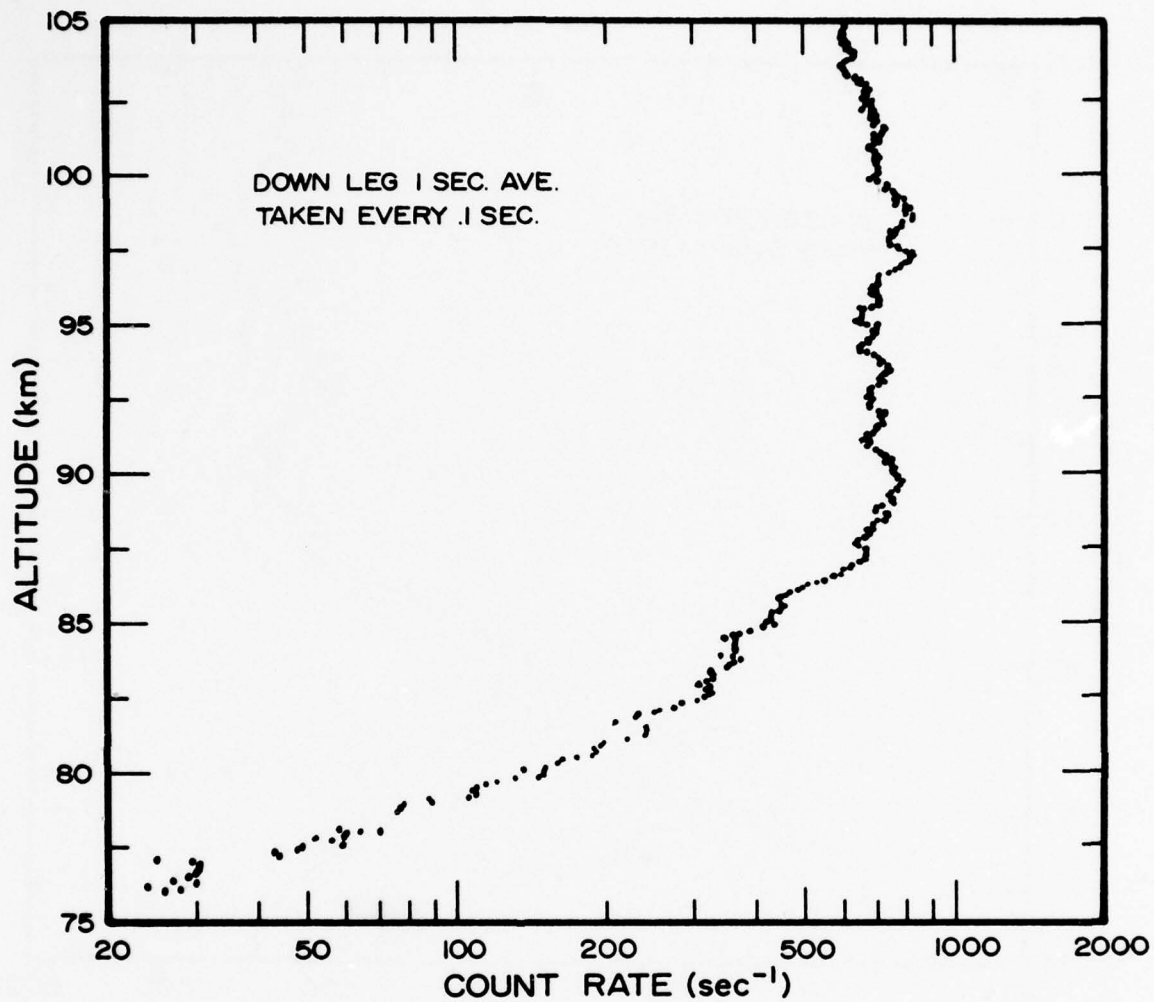


Figure 37. High resolution down leg data showing less structure than up leg. Data reduced with 1 second running average taken every .1 second.

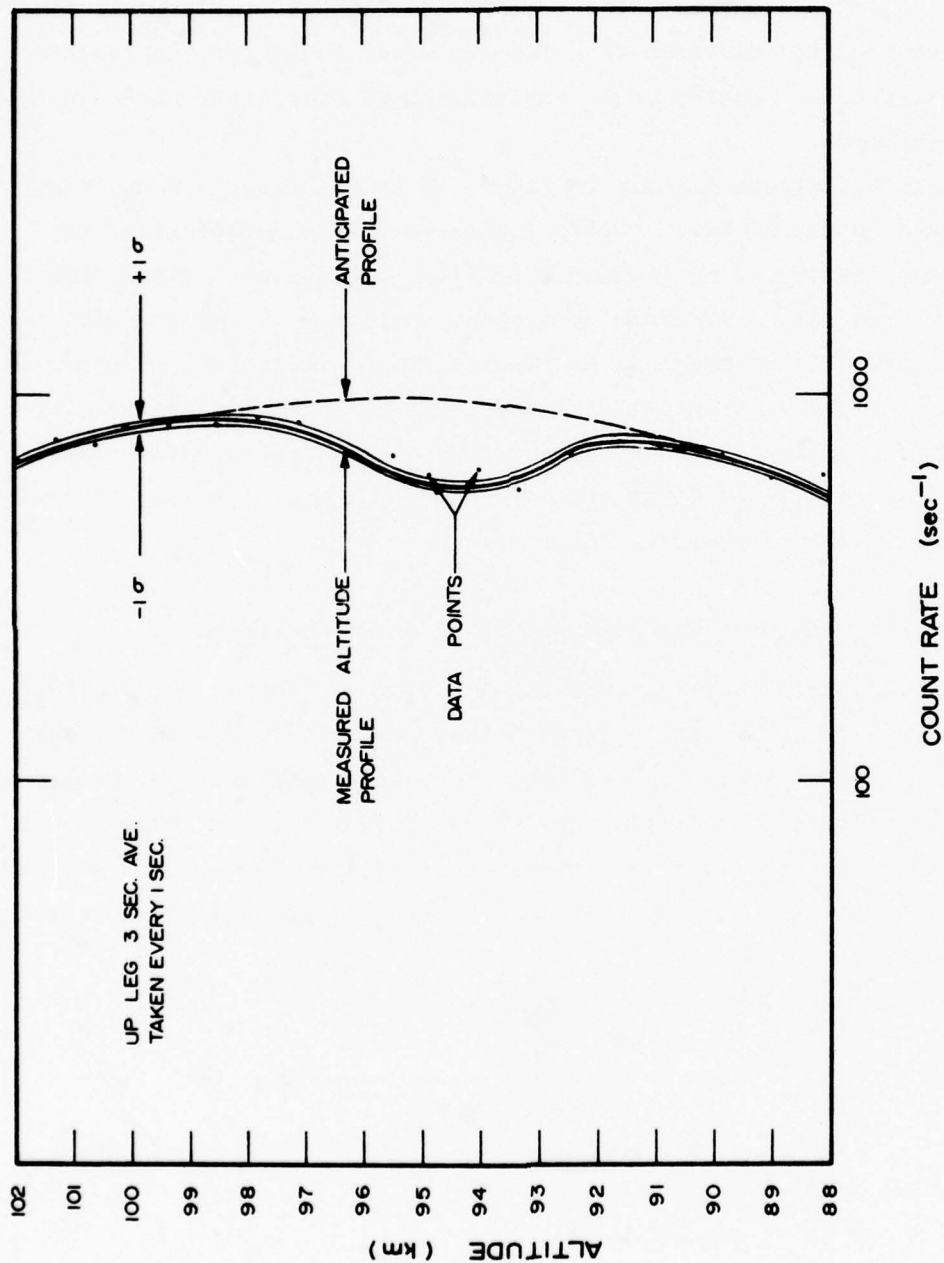


Figure 38. Statistical significance of 84 km dip in 0 density illustrated by $\pm 1\sigma$ limits in 0 density based on count rate statistics and a smooth curve which might have been expected which is many σ outside the measurement.

density profile without a dip. Deviations of plus and minus one standard deviation (σ) are shown based on the count rates and integration times. Obviously the dip in density at ~ 94 km cannot be considered anything but real based on statistical deviations since the "smooth" anticipated curve is many σ outside the measurements. The dip must, therefore, represent a real valley in the O density or be explainable by some other unrecognized physical phenomena.

A comparable approach shown in Figure 39 to the structure which appears between 80 and 90 km on the up leg shows similar statistical evidence for the reality of structured O density, but not with the strength exhibited at the higher altitude. As shown in Figure 40 for the altitude between 110 and 120 km, there is no statistical argument for any structure other than a purely exponential decrease in density with altitude. There is also little argument for significant fine scale structure in O density in the downleg data below 90 km which is not too surprising from the relatively smooth profile shown in Figure 37.

Comparison with Ground-based 557.7 nm Measurements

A well-calibrated vertical viewing 557.7 nm photometer was provided at the launch site to provide a simultaneous comparison between the measured atomic oxygen profile as derived from flight data and the integrated column emission rate from O(¹S). During the flight time of the O payload the measured O(¹S) emissions were recorded at 93 Rayleighs, which was comparatively low for the approximately one week period during which measurements were taken.

The O(¹S) intensity was calculated from

$$I = \frac{A K_1 [O]^3}{A + K_2 [O] + K_3 [M]}$$

where $K_1 = 1.4 \times 10^{-30} \exp(-1300/RT)$

$K_2 = 5.0 \times 10^{-11} \exp(-610/RT)$

$K_3 = 6.1 \times 10^{-}$

$A = .72$

which takes into account deactivation from both O and all other molecular species. The rate coefficients were derived from recent measurements by

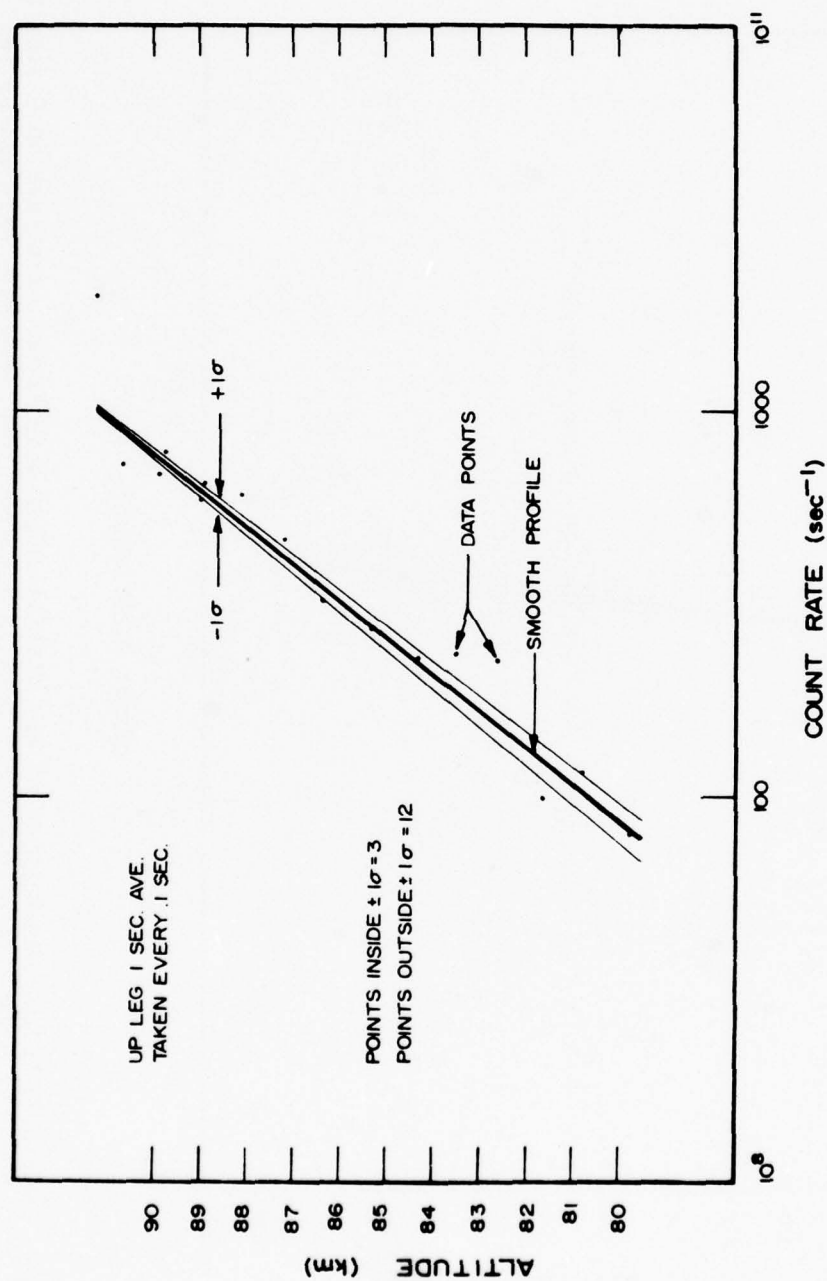


Figure 39. Illustration of significance of structure in up leg profile based on far too many data points existing outside $\pm 1\sigma$ from a smooth anticipated curve.

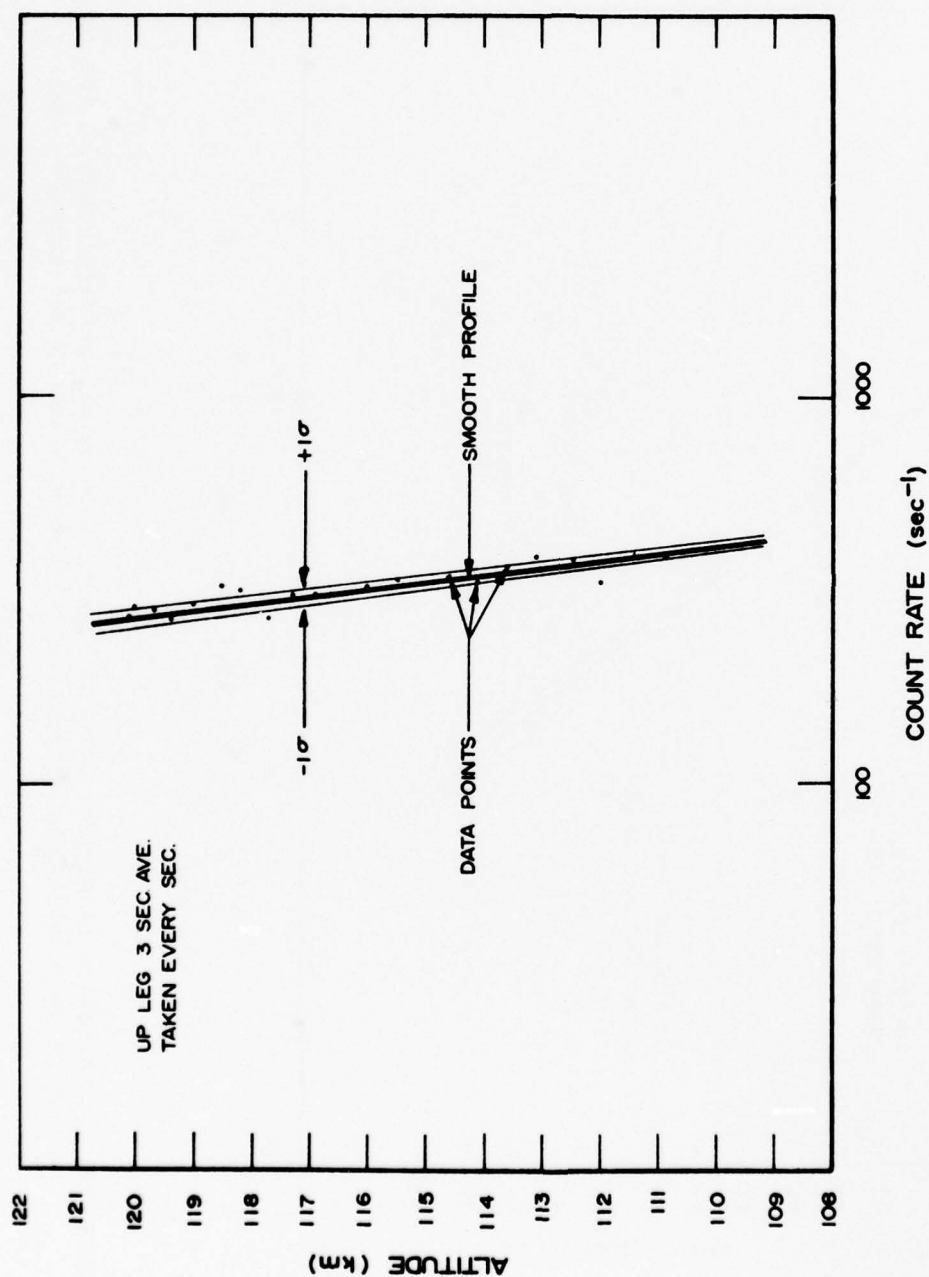


Figure 40. Illustration of the absence of any statistically significant structure in 0 density above the peak. This is true of both up and down legs, although only the up leg is shown.

[Slanger and Black, 1976] along with models for temperatures and member density profiles. The volume emission rates were calculated from the measured sounding rocket results for $[O]$ at 1 km intervals. The resulting emission profile was then integrated and compared with the ground-based $O(^1s)$ measurement. When this comparison was made, a scaling factor of approximately 1.3 was required to produce equal intensities. Figure 41 shows the computed and scaled volume emission rate for the up-leg portion of the night flight along with the integrated intensity.

The absence of obvious structure in the integral curve illustrates the value of an *in situ* measurement any time structure of small scale size may be present. It would be very difficult to obtain an accurate O altitude profile by differentiating an integral measurement of $O(^1s)$ from a rocket-borne instrument, especially since a vertical emission profile is difficult to obtain from a sounding rocket which is free from significant effects of the vehicle motion (spin coning, etc.).

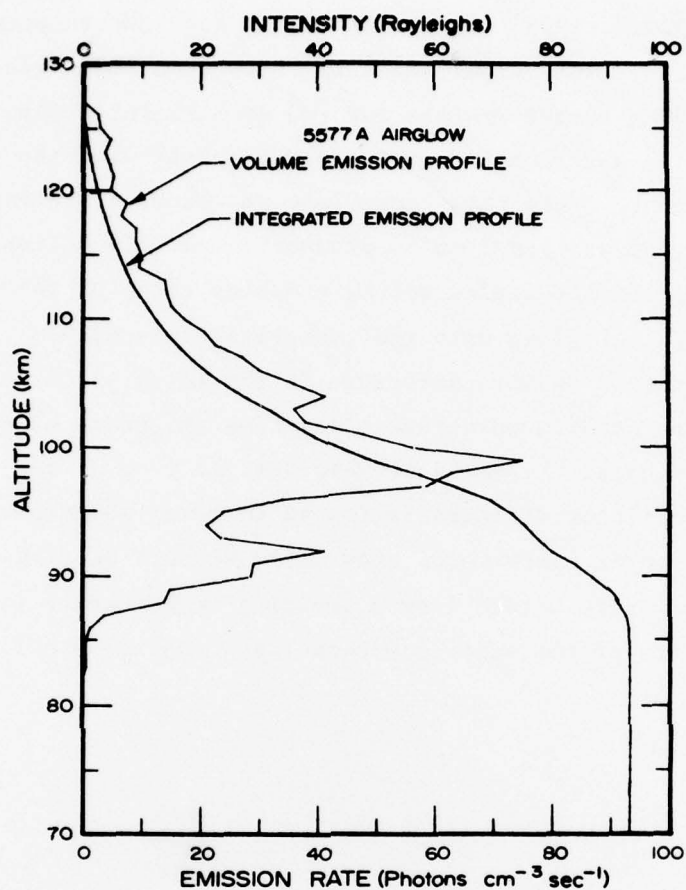


Figure 41. Volume emission rate and integrated column intensity of 557.7 nm $O(^1S)$ radiation during the flight time of Astrobee D A30.41304.

REFERENCES

- Fastie, W.G., H.M. Crosswhite, and D.F. Heath, Rocket spectrophotometer airglow measurements in the far ultraviolet, *J. Geophys. Res.*, 69, 19, 4129, October 1964.
- Fastie, W.G., Far ultraviolet day airglow studies, *Planet. Space Sci.*, 16, 7, 929, July 1968.
- Hicks, G.T. and T.A. Chubb, Equatorial aurora/airglow in the far ultraviolet, *J. Geophys. Res.*, 75, 31, 6233, November 1970.
- Peek, H.M., Vacuum ultraviolet emission from auroras, *J. Geophys. Res.*, 75, 31, 6209, November 1970.
- Samson, J.A.R., *Techniques of Vacuum Ultraviolet Spectroscopy*, John Wiley & Sons, Inc., New York, 1967.
- Slanger, T.G. and G. Black, $O(^1S)$ production from oxygen atom recombination, *J. Chem. Phys.*, 64, 9, 3767, May 1976.
- Slanger, T.G. and G. Black, $O(^1S)$ quenching by $O(^3P)$, *J. Chem. Phys.*, 64, 9, 3763, May 1976.
- Strickland, D.J. and T.M. Donahue, Excitation and radiative transport of OI 1304A resonance radiation, *Planet. Space Sci.*, 18, 5, 661, May 1970.

APPENDIX A

Program 1

Program for the Numerical Evaluation
of the Resonant Scattering Geometry for A30.413-4 and 5

```

100 C* TITLE: MAIN MODEL PROGRAM.....MODEL
200 C*
300 C*
400 C* STATEMENT OF VARIABLES:
500 C*
600 C* MINPT: PT OF MIN DISTANCE WHERE SOURCE FIELD
700 C* OF VIEW CROSSES DETECTOR FIELD OF VIEW
800 C* STHETA: TRANSLATION ANGLE TO SOURCE
900 C* DTHETA: TRANSLATION ANGLE TO DETECTOR
1000 C* SXDIST: DISTANCE FM SOURCE TO MINPT IN 'X' DIR
1100 C* SYDIST: DISTANCE FM SOURCE TO MINPT IN 'Y' DIR
1200 C* DXDIST: DISTANCE FM DETECTOR TO MIN PT IN 'X' DIR
1300 C* OX: ATOMIC OXYGEN DENSITY (CM-3)
1400 C* SPHOT: SOURCE INTENSITY (PHOTONS/SEC-SR)
1500 C* EPHOT: EMITTER (OXYGEN ATOMS) INTENSITY
1600 C* DPHOT: DETECTED INTENSITY
1700 C* SR: DISTANCE FM SOURCE TO INTEGRATING ELEMENT
1800 C* DR: DISTANCE FM DETECTOR TO INTEGRATING ELEMENT
1900 C* SPHI: ANGLE FM SOURCE TO INTEGRATING ELEMENT
2000 C* DPHI: ANGLE FM DETECTOR TO INTEGRATING ELEMENT
2100 C* AS: AREA OF SPHERE WITH RADIUS DR
2200 C* AD: AREA OF DETECTOR
2300 C* D: INCREMENT STEP SIZE FOR INTEGRATION (CM)
2400 C* DIS: MAX DISTANCE FM DETECTOR FOR INTEGRATION (CM)
2500 C* SRAD: RADIUS OF SOURCE
2600 C* SAPRAD: SOURCE APERTURE RADIUS
2700 C* DRAD: RADIUS OF DETECTOR
2800 C* DAPRAD: DETECTOR APERTURE RADIUS
2900 C* ASDIST: DISTANCE FM SOURCE TO SOURCE APERTURE
3000 C* ADDIST: DISTANCE FM DETECTOR TO DETECTOR APERTURE
3100 C* SIGMA: ABSORPTION CROSS SECTION
3200 C* DF: ARRAY OF CONVOLUTED VALUES USED TO DETERMINE
3300 C* DETECTION AS A FUNCTION OF ANGLE
3400 C* SF: ARRAY OF CONVOLUTED VALUES USED TO DETERMINE
3500 C* SOURCE INTENSITY AS A FUNCTION OF ANGLE
3600 C* SMAXA: SOURCE MAX ANGLE FOR SUBROUTINE CNVFN
3700 C* SMINA: SOURCE MIN ANGLE " " "
3800 C* DMAXA: DETECTOR MAX ANGLE " " "
3900 C* DMINA: DETECTOR MIN ANGLE " " "
4000 C* SA/DA: SOURCE/DETECTOR ANGLE ARRAY
4100 C* BLAMPA: ANGLE AT WHICH LAMP OUTPUT IS ZERO
4200 C*
4300 C*
4400 C* DIMENSION DF(53), SF(53), SA(53), DA(53)
4500 C* COMMON CS,SS,CD,SD,PI,DXDIST,SXDIST,SYDIST
4600 C* SMAXA = 0.5428
4700 C* SMINA = 0.0864
4800 C* DMAXA = 0.1292
4900 C* DMINA = 0.1047
5000 C* SIGMA = 3.43E-14
5100 C* BLAMPA = 0.5585
5200 C* AD = 7.07E-2
5300 C* PI = 3.141592654
5400 C* STHETA = -.3927

```

Program 1 (cont.)

```

5500      DTHETA = -.1309
5600      CS = COS(DTHETA)
5700      CD = COS(DTHETA)
5800      SS = SIN(DTHETA)
5900      SD = SIN(DTHETA)
6000      SXDIST = 2.62
6100      SYDIST = 3.00
6200      DXDIST = 12.52
6300      ASDIST = 1.82
6400      ADDIST = 9.70
6500      SRAD = 0.5
6600      SAPRAD = 0.65
6700      DRAD = 0.15
6800      DAPRAD = 1.15
6900      CALL CNVFN(SRAD,SAPRAD,ASDIST,SMINA,SMAXA,SF)
7000      CALL CNVFN(DRAD,DAPRAD,ADDIST,DMINA,DMAXA,DF)
7100      WRITE(6,401)
7200      READ(5,/)OX,SPHOT,D,DIS
7300      WRITE(6,402)
7400      1 SUM = 0.0
7500      PSUM = 0.0
7600      OV = 0.0
7700      TV = 0.0
7800      XX = 0.125
7900      X = 0.0
8000      Y = 0.0
8100      Z = 0.0
8200      J = SMAXA/50.0
8300      R = DMAXA/50.0
8400      SA(1) = 0
8500      JA(1) = R
8600      DO 2 I=2,52
8700      JA(I) = DA(I-1) + R
8800      2 SA(I) = SA(I-1) + Q
8900      5 CALL SCONE(X,Y,Z,SR,SPHI)
9000      ASPHI = ABS(SPHI)
9100      IF (ASPHI.GT.SMAXA) GO TO 15
9200      CALL DCONE(X,Y,Z,DR,DPHI)
9300      ADPHI = ABS(DPHI)
9400      IF (ADPHI.GT.DMAXA) GO TO 15
9500      10 I = 50.*ASPHI/SMAXA
9600      J = 50.*ADPHI/DMAXA
9700      IF (I.LT.1) FS = 1.0
9800      IF (I.LT.1) GO TO 13
9900      12 FS = ((SA(I+1)-ASPHI)*SF(I+1)+(ASPHI-SA(I))*SF(I))/Q
10000      13 IF (J.LT.1) FD = 1.0
10100      IF (J.LT.1) GO TO 14
10200      FD = ((DA(J+1)-ADPHI)*DF(J+1)+(ADPHI-DA(J))*DF(J))/R
10300      14 EPHOT = SPHOT*OV*OX*COS(SPHI)*SIGMA/(SR*SR)
10400      BLOUT = (BLAMPA - ASPHI)/BLAMPA
10500      XXXX = OX*SIGMA
10600      SNLS = XXXX*SR
10700      JNLS = XXXX*DR
10800      EPHOT = FS*EPHOT*EXP(-SNLS)*BLOUT
10900      AS = 4*PI*DR*DR
11000      JPHOT = EPHOT*FD*(AD/AS)*EXP(-DNLS)
11100      SUM = SUM + 2.0*DPHOT
11200      PSUM = PSUM + 2.0*DPHOT
11300      Z = Z + D
11400      TV = TV + 2.0*DV
11500      GO TO 5
11600      15 Y = Y - D
11700      Z = 0.0
11800      CALL SCONE(X,Y,Z,SR,SPHI)
11900      ASPHI = ABS(SPHI)

```

Program 1 (cont.)

```

12000      IF (ASPHI.GT.SMAXA.AND.Y.GE.-D) GO TO 20
12100      IF (ASPHI.GT.SMAXA) GO TO 26
12200      19 CALL DCONE(X,Y,Z,DR,DPHI)
12300      ADPHI = ABS(DPHI)
12400      IF (ADPHI.GT.DMAXA) GO TO 25
12500      GO TO 10
12600      20 Y = Y - D
12700      CALL SCONE(X,Y,Z,SR,SPHI)
12800      ASPHI = ABS(SPHI)
12900      IF (ASPHI.GT.SMAXA.AND.X.GT.5.0) GO TO 20
13000      GO TO 19
13100      25 IF (PSUM.LT.0.0001*SUM) GO TO 40
13200      IF (X.GE.2.0*XX) GO TO 35
13300      26 X = X + D
13400      Y = 0.0
13500      Z = 0.0
13600      CALL SCONE(X,Y,Z,SR,SPHI)
13700      CALL DCONE(X,Y,Z,DR,DPHI)
13800      ASPHI = ABS(SPHI)
13900      ADPHI = ABS(DPHI)
14000      PSUM = 0.0
14100      IF (X.GT.(DIS-DXDIST)) GO TO 40
14200      GO TO 10
14300      35 D = 2.0*D
14400      DV = D*D*D
14500      AX = X
14600      GO TO 26
14700      40 XP = (X + DXDIST - D)*CD
14800      WRITE(6,403)SUM,TV,XP
14900      DIS = DIS + 5.0*D
15000      GO TO 5
15100      STOP
15200      401 FORMAT(' INPUT IN FREE FORMAT: OX, SPHOT, D, AND DIS')
15300      402 FORMAT(' TOTAL COUNTS/SEC=',7X,' VOLUME=',6X,
15400      * 'DISTANCE FM DET.=',)
15500      403 FORMAT(4X,F12.3,3X,F14.3,8X,F8.2)
15600      END
15700      C*
15800      C*
15900      SUBROUTINE SCONE(X,Y,Z,SR,SPHI)
16000      C* THIS SUBROUTINE CONVERTS TO POLAR NOTATION CENTERED
16100      C* AT THE SOURCE
16200      COMMON CS,SS,CD,SD,PI,DXDIST,SDXDIST,SYDIST
16300      XF = X + SDXDIST
16400      YF = Y - SYDIST
16500      XP = XF*CS + YF*SS
16600      YP = -XF*SS + YF*CS
16700      XP = XP*XP
16800      YP = YP*YP
16900      ZP = Z*Z
17000      SR = SQRT(XP + YP + ZP)
17100      QX = SQRT(YP + ZP)
17200      SPHI = ARSIN(QX/SR)
17300      RETURN
17400      END
17500      C*
17600      SUBROUTINE DCONE(X,Y,Z,DR,DPHI)
17700      C* THIS SUBROUTINE CONVERTS TO POLAR NOTATION CENTERED
17800      C* AT THE DETECTOR
17900      COMMON CS,SS,CD,SD,PI,DXDIST,SDXDIST,SYDIST
18000      XF = X + DXDIST

```


Program 1 (cont.)

```

18100      XP = XF*CD + Y*SD
18200      YP = -XF*SD + Y*CD
18300      XP = XP*XP
18400      YP = YP*YP
18500      ZP = Z*Z
18600      JR = SQRT(XP + YP + ZP)
18700      JX = SQRT(YP + ZP)
18800      JPHI = ARSIN(OX/CR)
18900      RETURN
19000      END
19100
19100  C*
19200      SUBROUTINE CNVFN(RD,RA,D,MINPHI,MAXPHI,F)
19300      DIMENSION F(52)
19400      REAL MINPHI,MAXPHI
19500  C*
19600  C*   THIS SUBROUTINE COMPUTES AN ARRAY OF VALUES, F, FOUND
19700  C*   BY CONVOLUTION BETWEEN PROJECTED AREA OF APERTURE AND
19800  C*   AREA OF DETECTOR.
19900  C*   STATEMENT OF VARIABLES:
20000  C*       RD=DETECTOR/SOURCE RADIUS
20100  C*       RA=APERTURE RADIUS>RD
20200  C*       D=DISTANCE BETWEEN APERTURE AND DETECTOR
20300  C*       MINPHI=MAX ANGLE FM NORMAL SO THAT DETECTOR
20400  C*           AREA LIES INSIDE PROJECTED APERTURE AREA
20500  C*       MAXPHI=MIN ANGLE FROM NORMAL WITH NO SIGNAL
20600  C*       HA, HD=SEGMENT WIDTHS OF APERTURE PROJ AND
20700  C*           DETECTOR RESPECTIVELY
20800  C*       X=DISTANCE FROM ORIGIN TO LINE BETWEEN POINTS
20900  C*           OF INTERSECTION
21000  C*       CPHI=ANGLE IN WHICH X = 0
21100  C*       XM=PROJECTED CENTER OF APERTURE
21200  C*       AINT=AREA OF INTERSECTION
21300  C*       AD=AREA OF DETECTOR
21400  C*       ADS=AREA OF DETECTOR SEGMENT
21500  C*       AAS=AREA OF APERTURE PROJ SEGMENT
21600  C*
21700      RD2 = RD*RD
21800      RA2 = RA*RA
21900      CPHI = ATAN(SQRT((RA2 - RD2)/(D*D)))
22000      PI = 3.141592654
22100      AD = PI*RD2
22200      PHI = 0.0
22300      DELPHI = MAXPHI/50.0
22400      F(1) = 1.0
22500      I = 2
22600  3 PHI = PHI + DELPHI
22700      IF (PHI.LE.MINPHI) GO TO 5
22800      IF (PHI.GT.MINPHI.AND.PHI.LT.CPHI) GO TO 10
22900      IF (PHI.GE.CPHI.AND.PHI.LE.MAXPHI) GO TO 25
23000      GO TO 40
23100  5 F(I) = COS(PHI)
23200      I = I + 1
23300      GO TO 3
23400  10 XM = TAN(PHI)*D
23500      A = XM/2.0 + (RD2 - RA2)/(2.0*XM)
23600      HA = RA - (XM - X)
23700      HD = RD + X
23800      ADS = RD2*ARCOS((RD-HD)/RD)-(RD-HD)*SQRT(2.*RD*HD-HD*HD)
23900      AAS = RA2*ARCOS((RA-HA)/RA)-(RA-HA)*SQRT(2.*RA*HA-HA*HA)
24000      AINT = AD - ADS + AAS
24100      F(I) = (AINT/AD)*COS(PHI)

```

Problem 1 (cont.)

```

24200      PHI = PHI + DELPHI
24300      I = I + 1
24400      IF (PHI.GE.CPHI) GO TO 25
24500      GO TO 10
24600  25  XM = TAN(PHI)*D
24700      X = XM/2.0 + (RD2 - RA2)/(2.0*XM)
24800      HA = X - (XM - RA)
24900      HD = RD - X
25000      ADS = RD2*ARCOS((RD-HD)/RD)-(RD-HD)*SQRT(2.*RD*HD-HD*HD)
25100      AAS = RA2*ARCOS((RA-HA)/RA)-(RA-HA)*SQRT(2.*RA*HA-HA*HA)
25200      AINT = AAS + ADS
25300      F(I) = (AINT/AD)*COS(PHI)
25400      PHI = PHI + DELPHI
25500      I = I + 1
25600      IF (PHI.GT.MAXPHI) GO TO 40
25700      GO TO 25
25800  40  RETURN
25900      END

```

Commutator Assignments

Format: 16 segment, NRZ 10 frames/sec

<u>Segment</u>	<u>Function</u>
1	Lamp temperature
2	Magnetometer bias
3	Door monitor (+1v on, +4v off)
4	Filter temperature
5	Pyro battery "A" monitor
6	Pyro battery "B" monitor
7	Payload temperature (on circuit card)
8	+28v
9	Lamp intensity
10	Lamp heater
11	High voltage (CEM)
12	0v
13	+5v
14	+5v
15	+5v
16	+2.5v

Telemetry Assignments

Transmitter: Type ----- Vector 102S
Power ----- 2 watts
Frequency -- 2269.5 MHz
Modulation - FM/FM

<u>IRIG Subcarrier</u>	<u>Input Voltage Range</u>	<u>Description</u>
19	-	O.S.U. ranging
18	0 - +5v	Lamp off data
17	"	Lamp on data
16	"	*Attitude sensor
15	"	16 segment commutator
12	"	Magnetometer

*IR horizon sensor used on A30.413-4, Bay Shore Systems Solar
aspect sensor used on A30.413-5.

DISTRIBUTION LISTDEPARTMENT OF DEFENSE

Director
 Defense Advanced Rsch. Proj. Agency
 Attn: LTC W.A. Whitaker

Defense Documentation Center
 Attn: TC (2 Copies)

Director
 Defense Nuclear Agency
 Attn: TITL Tech. Library (3 Copies)
 Attn: TISI Archives
 Attn: RAEV Harold C. Fitz, Jr.
 Attn: RAAE Maj. J. Mayo
 Attn: RAAE G. Soper
 Attn: RAAE Maj. R. Bigoni

Dir. of Defense Rsch. & Engineering
 Department of Defense
 Attn: DD/S&SS (OS) Daniel Brockway

Commander
 Field Command
 Defense Nuclear Agency
 Attn: FCPR

Chief Livermore Division
 FLD Command DNA
 Attn: FCPRL

DEPARTMENT OF THE ARMY

Commander/Director
 Atmospheric Sciences Laboratory
 U.S. Army Electronics Command
 Attn: DRSEL-BL-SY-A.F. Miles
 Attn: H. Ballard

Commander
 Harry Diamond Laboratories
 Attn: DRXDO-NP, F.H. Alminetz (2 Copies)

Commander
 U.S. Army Nuclear Agency
 Attn: Mona-We

Director
 BMD Advanced Technical Center
 Attn: ATC-T, M. Capps
 Attn: ATC-O, W. Davies

Dep. Chief of Staff for Rsch, Dev & Acout.
 Department of the Army
 Attn: MCB Division
 Attn: DAMA-CSZ-C
 Attn: DAMA-WSZC

Director
 U.S. Army Ballistic Rsch Labs.
 Attn: John Mester
 Attn: Tech. Library

Commander
 U.S. Army Electronics Command
 Attn: Inst. for Expl. Research
 Attn: Weapons Effects Section

Commander
 CORADCOM
 Attn: PP-Library

DEPARTMENT OF THE NAVY

Commander
 Naval Oceans Systems Center
 Attn: Code 2200 William Moler

Director
 Naval Research Laboratory
 Attn: Code 7712 D.P. McNut
 Attn: Code 6701 J.D. Brown
 Attn: Code 2600 Tech. Library
 Attn: Code 7175J C.Y. Johnson
 Attn: Code 6700 T.P. Coffey
 Attn: Code 7709 Wahab Ali
 Attn: Code 6780 D.F. Strobel
 Attn: Code 6780 P. Julienne
 Attn: Code 67800 J. Fedder
 Attn: Code 6780 S. Ossakow
 Attn: Code 6707 J. Davis

Commander

Naval Surface Weapons Center

Attn: Code WA 501 Navy NUC Prgms. Off.

Attn: Technical Library

Superintendent

Naval Post Graduate School

Attn: Rech Rpts Librarian

Commander

Naval Intelligence Support Ctr

Attn: Document Control

DEPARTMENT OF THE AIR FORCE

AF Geophysics Laboratory, AFSC

Attn: LKB, K.S.W. Champion

Attn: OPR, A.T. Stair, Jr.

Attn: OPR, P.G. Doyle

Attn: OPR, R. Murphy

Attn: LKO, R. Huffman

AF Weapons Laboratory, AFSC

Attn: Maj. Gary Ganong, DES

Commander

ASD

Attn: ASD-YH-EX-LTC R. Leverette

SAMSO/AW

Attn: SZJ Lt. Col. Doan

SAMSO/YN

Attn: Maj. P. Sivgals

AFTAC

Attn: Tech Library

Attn: TD

HQ

Air Force Systems Command

Attn: DLS

Attn: Tech Library

Attn: DLCAE

Attn: DLTW

Attn: DLXP

Attn: SDR

Attn: RDQ

US ENERGY RSCH. and DEV. ADMIN.

Division of Military Application

U.S. Energy Rsch & Dev Admin

Attn: Doc. Con.

Los Alamos Scientific Laboratory

Attn: DOC CON for H.V. Argo

Attn: DOC CON for M.B. Pongratz

Attn: DOC CON for R. Brownlee

Attn: Group AP-4, MS 567

Attn: DOC CON for J. Zinn

University of California

Los Alamos Scientific Laboratory

Attn: Librarian MS 362

Sandia Laboratories

Attn: DOC CON for W.B. Brown, Org. 1353

Attn: Tech. Library, Org. 3141

Argonne National Laboratory

Records Control

Attn: Doc. Con. for D.W. Green

Attn: Doc. Con. for LIR SVCS Rpts Sec

Attn: Doc. Con. for G.T. Reedy

University of California

Lawrence Livermore Laboratory

Attn: W.H. Duewer, L-262

Attn: J. Chang, L-71

U.S. Energy Rsch & Dev. Admin

Division of Headquarters Services,

Library Branch

Attn: Doc. Con. for Class. Tech. Lib.

OTHER GOVERNMENT

Department of Transportation

Office of the Secretary

Attn: S.C. Coroniti

NASA

Goddard Space Flight Center

Attn: Code 6801 A. Temkin

Attn: Tech. Library

Attn: Code 900 J. Siry

NASA

Langley Station

Attn: Tech. Library

NASA

Ames Research Center

Attn: N-245-3 R. Whitten

Department of the Army

Bal. Miss. Def. Adv. Tech. Ctr.

Attn: W.O. Davies

Federal Aviation Administration
Attn: EAPP/AEQ-10/James W. Rogers

Central Intelligence Agency
Attn: ED/SI RM 5G48 HQ Bldg.
Attn: NED/OS I-2G4R HQS

Department of Commerce
National Bureau of Standards
Attn: Sec. Officer for M. Krauss
Attn: Sec. Officer for L.H. Gevantman

National Oceanic & Atmospheric Admin.
Environmental Research Laboratories
Department of Commerce

Attn: G. Reid
Attn: E. Ferguson
Attn: F. Fehsenfeld

DEPARTMENT OF DEFENSE
CONTRACTORS

Science Applications Inc.
Attn: D.G. Kopper

Aero-Chem Research Laboratories, Inc.
Attn: A. Fontijn
Attn: H. Pergament

Aerodyne Research, Inc.
Attn: F. Bien
Attn: M. Canac

Aerospace Corporation
Attn: N. Cohen
Attn: H. Mayer
Attn: R.J. McNeal
Attn: T.D. Taylor
Attn: J. Reinheimer
Attn: R.D. Rawcliffe

AVCO-Everett Research Laboratory Inc.
Attn: Tech. Library
Attn: C.W. Von Rosenberg, Jr.

Battelle Memorial Institute
Attn: H.L. Lamuth
Attn: STOIAC

Brown Engineering Company, Inc.
Attn: N. Passino

General Research Corporation
Attn: D. Jones

California At Riverside, University of
Attn: J.N. Pitts, Jr

California at San Diego, University of
Attn: S.C. Lin

California University of Berkeley
Attn: Sec. Officer for H. Johnston
Attn: Sec. Officer for Dept of Chem.,
H.L. Strauss

Calspan Corporation
Attn: C.E. Treanor
Attn: J.M. Grace
Attn: M.G. Dunn
Attn: W. Wurster

University of Colorado
Astro-Geophysics
Attn: J.B. Pearce

Colorado, University of
Office of Contracts and Grants
Attn: G.M. Lawrence, LASP

Concord Sciences
Attn: E.A. Sutton

University of Denver
Space Science Laboratory
Attn: B. Van Zyl

University of Denver
Denver Research Laboratory
Attn: Sec. Officer for D. Murcray

General Electric Company
Tempo-Center for Advanced Studies
Attn: DASAIC
Attn: W.S. Knapp
Attn: T. Stephens
Attn: D. Chandler
Attn: V.R. Strull

General Electric Company
Space Division
Attn: M.H. Bortner, Space Science Lab.
Attn: J. Burns
Attn: F. Alyea
Attn: P. Zavitsands
Attn: R.H. Edsall
Attn: T. Baurer

General Research Corporation

Attn: J. Ise, Jr.

Geophysical Institute

University of Alaska

Attn: J.S. Wagner

Attn: M. Brown

Lowell University of

Center for Atmospheric Research

Attn: G.T. Best

Lockheed Missiles and Space Company

Attn: J. Kumer, Dept. 52-54

Attn: J.B. Cladis, Dept 52-12, B202

Attn: B.M. McCormac, Dept. 52-54

Attn: T. James, Dept. 52-54

Attn: M. Walt, Dept. 52-10

Attn: R.D. Sears, Dept. 52-54

Institute for Defense Analysis

Attn: E. Bauer

Attn: H. Wolfhard

Mission Research Corporation

Attn: D. Archer

Attn: D. Fischer

Attn: M. Scheibe

Attn: D. Sappenfield

Attn: D. Sowle

Photometrics, Inc.

Attn: I.L. Kofsky

Berkeley Research Associates

Attn: J.B. Workman

Physical Dynamics Inc.

Attn: A. Thompson

Physical Sciences, Inc.

Attn: K. Wray

Attn: R.L. Taylor

Attn: G. Caledonia

Physics International Company

Attn: Doc Con for Tech Library

Pittsburgh, University of the Comwlth
System of Higher Education

Attn: W.L. Fite

Attn: M.A. Biondi

Attn: F. Kaufman

R & D Associates

Attn: R. Latter

Attn: R.G. Lindgren

Attn: B. Gabbard

Attn: R. Lelevier

Attn: A.L. Latter

Attn: F. Gilmore

Attn: E.J. Mitchell

Rand Corporation

Attn: C. Crain

Science Applications, Inc.

Attn: D.A. Hamlin

Attn: D. Sachs

Stanford Research Institute International

Attn: M. Baron

Attn: W.G. Chesnut

Technology International Corporation

Attn: W.P. Boquist

United Technologies Corporation

Attn: H. Michels

Attn: R.H. Bullis

Utah State University

Attn: D. Baker

Attn: K. Baker

Attn: C. Wyatt

Attn: A. Steed

Visidyne, Inc.

Attn: H. Smith

Attn: J.W. Carpenter

Attn: T.C. Degges

Attn: C. Humphrey

Wayne State University

Attn: R.H. Kummaler

Attn: W.E. Kaupplia

Commander

Rome Air Development Center

Attn: OSCA, J.J. Simons

Stewart Radiance Laboratory

Attn: R. Huppi

Boston College

Space Data Analysis Laboratory

Attn: E.R. Hegblom

Attn: W.F. Grieder

Forrestal Campus Library

Princeton Univeristy

Attn: Librarian

Printed by
United States Air Force
Hanscom AFB, Mass. 01731